Measurement of charged D*+ meson production in Pb-Pb collisions in 60-80% centrality with the ALICE detector at CERN

Author
Stan Oomen
Utrecht University
Student number - 4000315

Supervisors
Dr. Alessandro Grelli
Utrecht University
Dr. Raimond Snellings
Utrecht University
Dr. André Mischke
Utrecht University

July 31, 2019

Abstract

The main goal of this thesis is to calculate the nuclear modification factor R_{AA} for prompt D^{*+} mesons in Pb-Pb data collected by the ALICE detector at CERN during the LHC run 2 at centre of mass energy $\sqrt{s_{NN}} = 5.02$ TeV in 2018. The reconstruction of the D^{*+} mesons was done by means of the hadronic decay channel $D^{*+} \rightarrow D^0 \pi^+ \rightarrow K^- \pi^+ \pi^+$ and its charge conjugate. Invariant mass, yield and the cross-section were measured in the transverse momentum interval $1 < p_T < 24$ GeV/c. The measured p_T differential cross section was compared to a p-p baseline to calculate the R_{AA} which is reported in this thesis. In the p_T range 4-12 GeV/c, a moderate suppression of the R_{AA} can be seen implying the formation of the Quark Gluon Plasma, a state of matter predicted by Quantum Chromo Dynamics. R_{AA} measurements from this thesis are compared to previous measurements by the ALICE collaboration. Furthermore, the measurements are compared to theoretical models.

Contents

Chapter 1

Introduction and motivation

The ALICE at the LHC is a dedicated detector to investigate the physics potential of nucleus-nucleus collisions at relativistic energies. Its general aim is to study the unknown physics that lies within the strongly interacting matter in extreme energy densities. This strongly deconfined matter is also referred to as a Quark Gluon Plasma which is formed at the LHC particle accelerator through ultra relativistic collisions.

The QGP is thought to be the state of matter at the early stages after the Big Bang at the birth of the universe. Also, the matter of the inner parts of neutron stars are suspected to have the same phase of matter. Understanding the Quark Gluon Plasma reveals much about the Quantum Chromo Dynamics, the theory behind the understanding of confinement and asymtotic freedom due to colour charge. By measuring hadrons, muons, electrons and photons that are produced in collisions with the ALICE detector, more insight is gained into the inner workings of the matter around us.

In this thesis, an observable called the nuclear modification factor (R_{AA}) is calculated from data on Pb-Pb collisions taken at the end of 2018 by the ALICE detector. This factor is given by the following and explained further in section 2.5.

$$R_{AA}(p_T) = \frac{dN_{AA}/dp_T}{\langle T_{AA} \rangle \cdot d\sigma_{pp}/dp_T} \tag{1.0.1}$$

A nuclear modification factor different than 1 indicates final state interactions of charm quarks with the Quark Gluon plasma.

Chapter 2 starts with a theoretical framework that is needed to understand the analysis. Then in chapter 3 the experimental setup of the ALICE detector at CERN is described. The actual analysis of the D^{*+} meson is described in chapter 4 including an in-depth investigation into the uncertainties. The last chapters 5 and 6 summarise the results and provide a discussion.

Chapter 2

Theoretical Overview

2.1 Standard Model

The ultimate goal of physicists is to unify all forces and particles that are present in the universe in one comprehensive model. An attempt at that is the Standard Model of physics which contains the building blocks for all matter that is currently known and also all forces that act between these particles except for gravity, as can be seen in the figure below. The first three columns are the particles and the two columns on the right consist of the force carriers.

The four currently known forces are mediated by their corresponding gauge bosons and are explained in the Standard model of Physics except for gravity. Gluons (g) carry the strong forces between particles with colour charge, $W^\pm$ and Z^0 bosons carry the weak interaction, photons (γ) carry the electromagnetic interaction and Higgs bosons and excitations of the Higgs field and responsible for giving other elementary particles mass due to a symmetry breaking. [1] Gravity is excluded in this model and in the scope of this thesis since it is too weak compared to the other forces to take into account. The particles can be divided into Quarks and Leptons, each in three generations with increasing mass and increasing instability.

While the Standard Model is verified experimentally with great accuracy, there are still many physical phenomena that are not explained by it. Dark matter and Dark energy are believed to make up around 95% of matter and energy in the universe, yet they are not incorporated into the Standard Model.[2] Furthermore, when the masses of quarks inside a proton or neutron are added up, they make up only 1/100 of the total mass, so it is largely unknown where the mass of these nucleons comes from. [3]
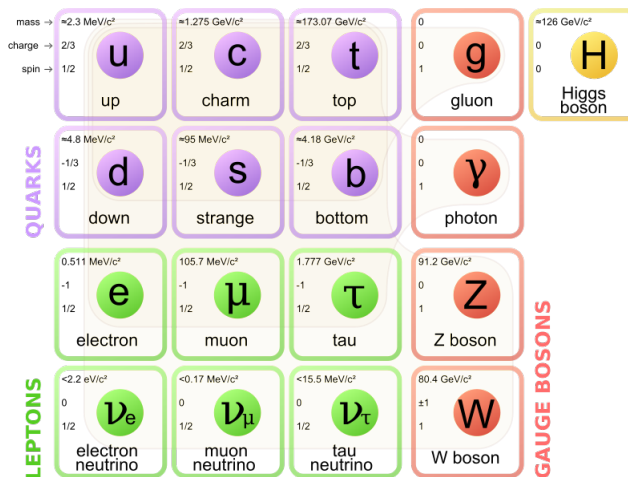

Figure 2.1 – The Standard Model of physics [5]

In this thesis, the focus lies mainly on one force of in the standard model namely the strong force and its force carrier, the gluon. These interactions are explained in the quantum field theory that is called Quantum Chromo Dynamics (QCD). Under conditions of extreme energy density and temperature, a phase transition from matter in which quarks and gluons are confined within hadrons to a deconfined state of matter called the Quark Gluon Plasma (QGP) happens. This state of matter is predicted by (Lattice-)QCD and can be produced with Relativistic Heavy-Ion collisions at CERN among other experiments.

2.2 Quantum Chromo Dynamics (QCD)

Quantum Chromo Dynamics (QCD) describes the dynamics of quarks and gluons and their strong interaction. [4] It is a non-Albelian quantum gauge field theory based on the invariance under local SU(3) group transformations. Where the electric charge has two different charges (+ and -), colour charge can assume three states: red, green and blue with their anti- counterparts (rgb and $\overline{rgb}$). All naturally visible particles are colour neutral. Hence a baryon such as the proton consist of two up quarks and a down quark (uud) which have colours red, green and blue. A meson such as the π^+ consist of an up quark and anti-quark pair (u$\overline{d}$). A quark has only one colour charge as supposed to a gluon which has two, a colour and an anti-colour charge. The fact that the gauge boson for the strong force self-interacts due to this makes it different from all other forces mentioned earlier.

The coupling constant in Quantum Chromo Dynamics depends on the distance between quarks in a much different way than in Quantum Electro Dynamics. Where in QED, the coupling becomes very large at short distances and smaller at longer distances, the coupling constant in QCD, α_s depends on the exchanged momentum (Q^2) which is inversely proportional to the spatial distance within which the interaction takes place. The interaction strength between two quarks behaves as follows.
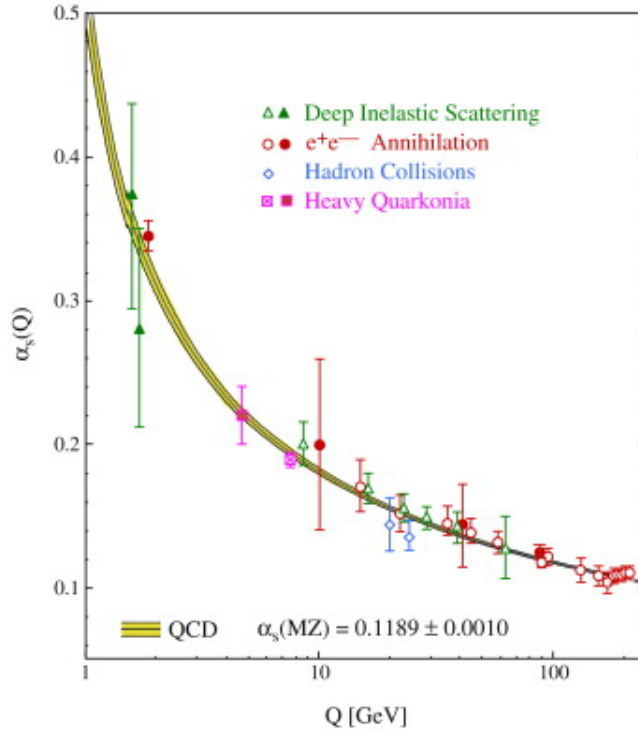
Figure 2.2 – The coupling factor in QCD as a function of exchanged momentum [6]

Which is approximated by the following formula:

$$\alpha_s(Q^2) = \frac{12\pi}{(33 - 2n_f)\ln(Q^2/\Lambda_{QCD}^2)}$$

(2.2.1)

With Λ_{QCD}^2 a dimensional parameter which represents the energy scale at which α_s diverges to infinity and n_f the number of quark families.

As can be seen from the figure above, large momentum transfer or small distances - α_s decreases to the point where partons can exist freely since the coupling constant decreases. This is called asymtotic freedom. For low momentum or large distances, α_s diverges. If we pull qq-bar apart, the binding energy and distance increases to a point where it is more favourable to produce another qq-bar pair from vacuum and split the original pair in two. This is called colour confinement.

2.3 Quark Gluon Plasma (QGP)

Asymtotic freedom as seen in the previous section gives motivation to investigate free partons within hadrons. The phase diagram of the QGP has been the object of research for several decades. As can be seen at high temperatures and density, a phase transition occurs. In this phase, partons move quasi-free throughout the medium called the Quark Gluon plasma. In addition, it is thought of to be the state of matter shortly after the Big Bang and inside neutron stars.

The conditions of high temperature and energy density needed to create a QGP have so far been met in heavy-ion collisions in particle accelerators such as at the LHC at CERN. In Pb-Pb collisions at nearly the speed of light, QGP like properties have been discovered after collisions. The lifetime of the QGP is extremely short since the system quickly expands and cools down. In this process, quarks and gluons recombine into hadrons. The hadrons that have been created in and have traversed through the QGP can be measured in detectors such as the ALICE detector.

Numerical calculations have predicted the formation of the QGP and indirect indications such as elliptic flow and production of particles containing strange quarks have provided proof of the QGP. However, there is no direct proof of the existence of the QGP since it is short-lived and too dense in energy to be measured directly.
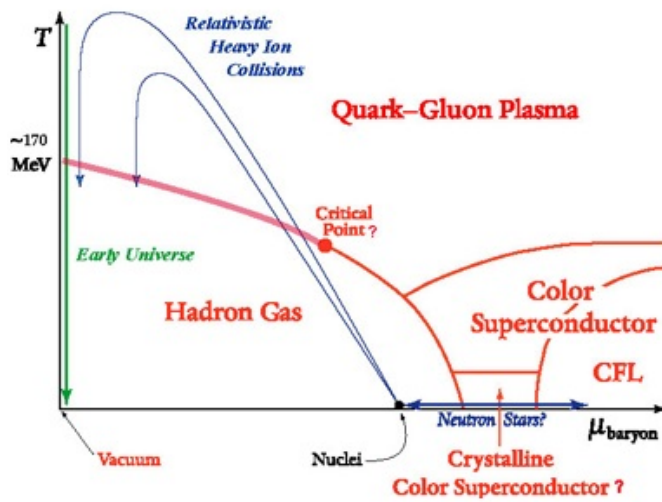

Figure 2.3 – Phase diagram of QGP including phase transitions [7]

2.4   Heavy flavour production

As mentioned in the previous paragraphs, the QGP matter cannot be measured directly. The only observables that can be analysed are the particles that reach the detector after the initial collision happened. Analysis of the type, transverse momentum or flow of the produced particles from the QGP reveals its inner properties. The properties of the particles are in turn determined by the cumulative effect of all the different phase contributions of the QGP. More on this in section 2.6 Collision development.

One of the most used probes for the properties of the QGP is the production of Heavy Flavour particles, namely particles that contain charm or beauty quarks, for instance D- or B mesons. For multiple reasons these are important in the investigation into the QGP.

Firstly, since the charm and beauty quarks are heavy, they are produced in the early stages of the collisions even before the QGP itself is formed, since the production time of the partons is inversely proportional to their mass. [8]. Secondly, the heavy quarks experience the complete evolution of the QGP system without decaying and lose less energy than lighter quarks due to colour charge and dead cone effects. [9] [10] Lastly, the heavy quarks are colour charged which makes them interact with the QGP. Overall, the heavy quarks have enough energy to traverse and survive the QGP phase and the resulting D- and B mesons (or their decay products) that contain these quarks still have properties that can be measured in the detector making them an excellent probe.
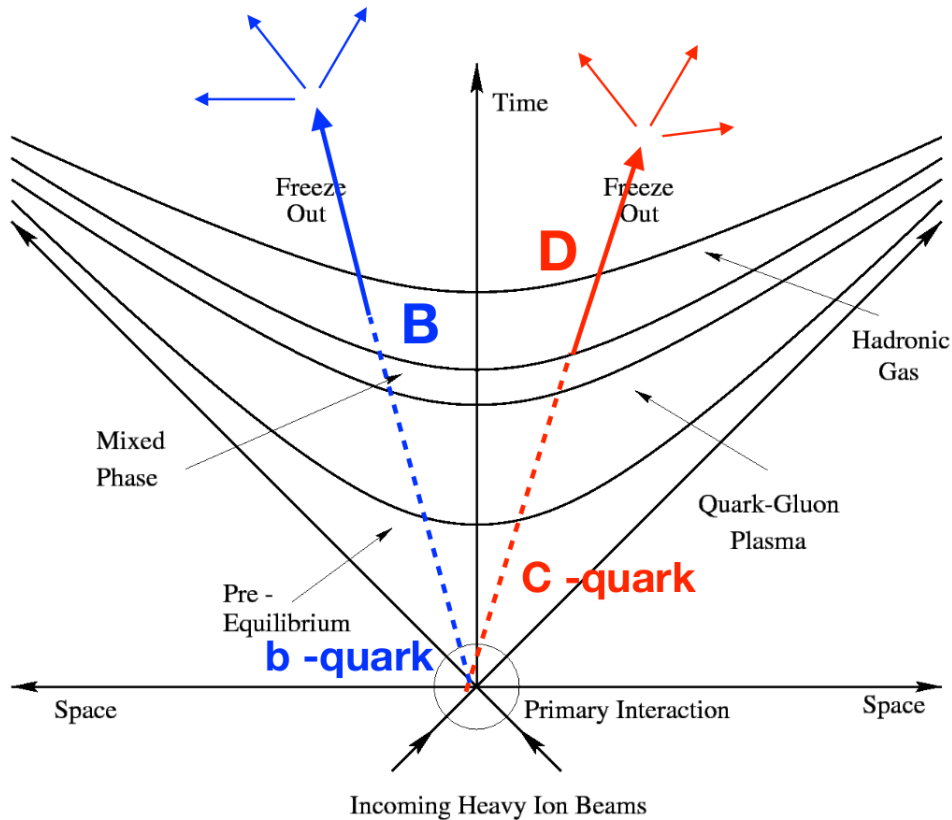

**Figure 2.4** – Creation of heavy quarks in the LHC experiment [11]

2.5   Observables

To gain knowledge on the physics that happens inside the collisions at the LHC there are two types of measurements that can be performed on the data: yields and correlations. Yield and specifically the distribution of particles with respect to p_T or pseudorapidity provides insight into the cross-section of the production process. Correlations are patterns in kinematic variables that contain the information on the interaction between specific particles such as elliptic flow. Since some of the collisions at the LHC are not head-on, peripheral collisions also take place. The two overlapping discs [1] of incoming particles form a volume shaped like an almond where particles do collide. The elliptic flow parameter v_2 describes the the momentum of heavy flavour particles after the initial collisions from this almond shape volume. In this thesis, only the yield and especially the ratio between yields in p-p and Pb-Pb is studied.

The main observable used in this thesis is the R_{AA} or the Nuclear Modification factor. It relies on the fact that heavy quarks that eventually form heavy flavour particles lose energy in the QGP medium. The ratio R_{AA} indicates whether the nuclear environment modifies the particle production through, for instance, energy loss. This factor is defined as the ratio of the differential yield in Pb-Pb collisions in a certain centrality class to the yield from a p-p cross-section scaled by a nuclear overlap function. [12] It is given as follows:

$$R_{AA}(p_T) = \frac{dN_{AA}/dp_T}{\langle T_{AA} \rangle \cdot d\sigma_{pp}/dp_T} \tag{2.5.1}$$

In this equation, N_{AA}/dp_T is the differential yield in heavy ion collisions, $\langle T_{AA} \rangle$ is the nuclear overlap function and $d\sigma_{pp}/dp_T$ is the cross-section in proton-proton collisions. This cross-section is used as a reference. An example of a measured R_{AA} can be seen in the following plot.

ALI-PUB-145228
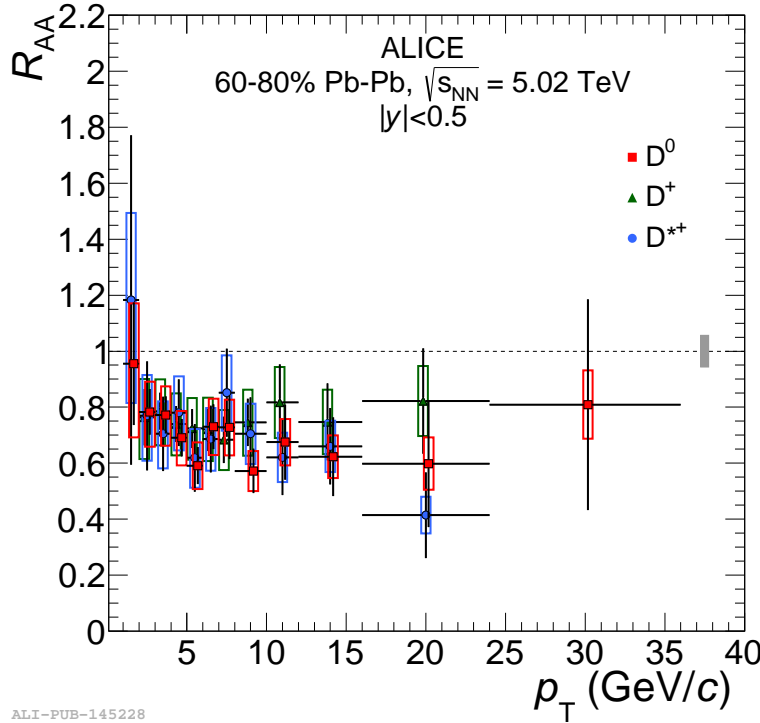
Figure 2.5 – Nuclear modification factor for different D-mesons in the 60-80 % centrality region [13]

---

[1] Due to relativistic effects in length contraction, the collision at relativistic speeds effectively happens between two flat discs of particles

As can be seen, a suppression of particles can be found in some p_T ranges as the R_{AA} is smaller than 1. This indicates nuclear effects on the produced D-mesons.

The main energy loss mechanisms are gluon radiation and parton collisions. Energy loss depends on a variety of factors including the QGP density, the path length in the QGP and species of parton that go through the medium. [14][15] Note that the ratio R_{AA} can be more than 1 since the differential yield distributions are shifted when Pb-Pb is compared to p-p. This gives rise to an $R_{AA} > 1$ for low p_T values.

2.6   Collision development

The collision between two lead nuclei in a particle collider at relativistic velocities results in a complex space-time evolution that can be categorised in several stages.

- **Collisions** The collision takes place in a very short time frame that is estimated to be around $\tau_{coll} \sim 0.1$ fm/c. The majority of the interactions that take place are by gluons since the Lorentz contracted nuclei can be described as most of the momentum is carried by the gluons before interaction.

- **QGP phase** When the QGP phase is reached, the system can be regarded as a relativistic fluid with a very low viscosity. Partons are indistinguishable from each other and acquire similar velocities in the expanding medium.

- **Freeze Out** When the overall temperature of the system drops below the critical temperature of $T_C = 155$ MeV, the individual partons start to hardronize into mesons again in a process that is called a chemical freeze-out. The loose hadrons scatter in all directions while the system keeps expanding. After this, the particles reach the detector elements to be analysed by the various detector elements.

The following picture shows the evolution of the various phases of the QGP from initial collision to eventual detection.
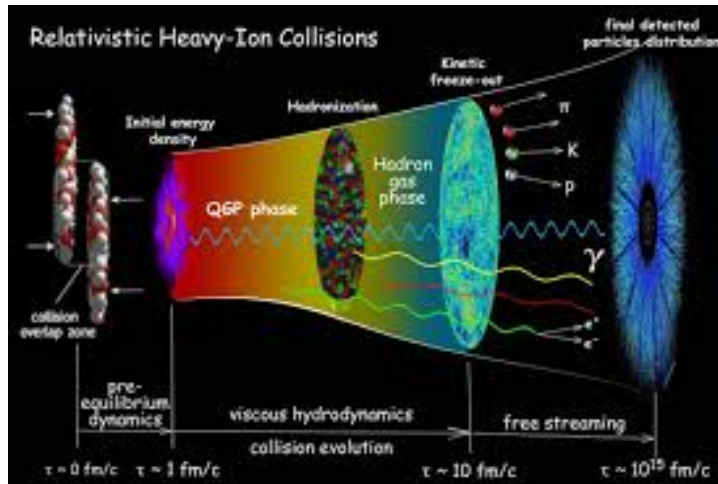

Figure 2.6 – QGP evolution after collision [16]

Chapter 3

Large Hardron Collider

3.1 Overview and Shutdown

The Large Hadron Collider (LHC) at CERN is currently the largest particle accelerator in the world. The main feature is a 27 kilometer long circle of superconducting magnets in which protons and lead ions are accelerated up to energies of $\sqrt{s} = 14$ TeV and $\sqrt{s_{\mathrm{NN}}} = 5.02$ TeV respectively.

Through multiple steps and accelerator parts, the protons and ions are accelerated to a velocity that is close to the speed of light. [17] Before the lead ions reach the final stage which is the LHC itself, they go through several phases of acceleration. Firstly, in LINAC3 lead ions are accelerated up to an energy of $\sqrt{s_{\mathrm{NN}}} = 50$ MeV. Subsequently, they are injected into LEIR which divides them into bunches that are suitable for the LHC. Then they pass through accelerators Proton Synchrotron (PS) and Super Proton Synchrotron (SPS) where they reach an energy of $\sqrt{s_{\mathrm{NN}}} = 450$ GeV. For the proton-proton reference used in this thesis, a similar acceleration scheme is used except they start at the LINAC 2. Then the beam reaches its ultimate energy as mentioned before in the LHC where the different detector experiments are placed along the beam in order to analyse the relativistic collisions.
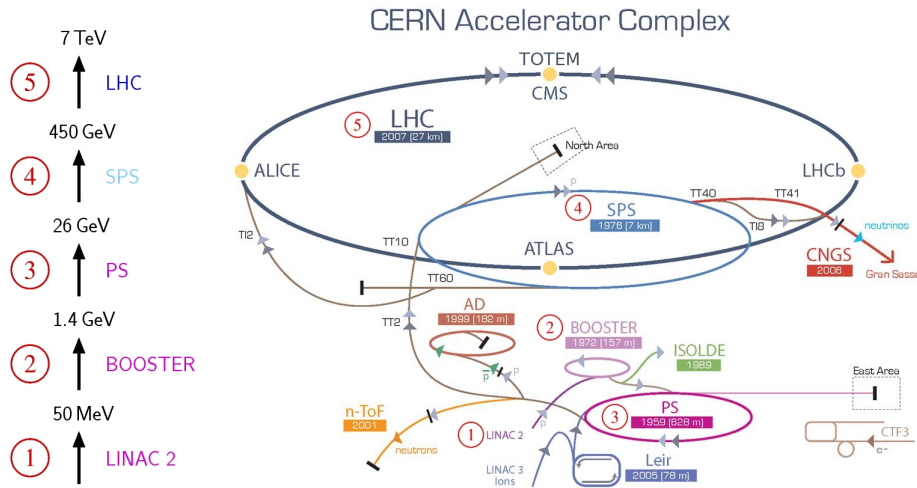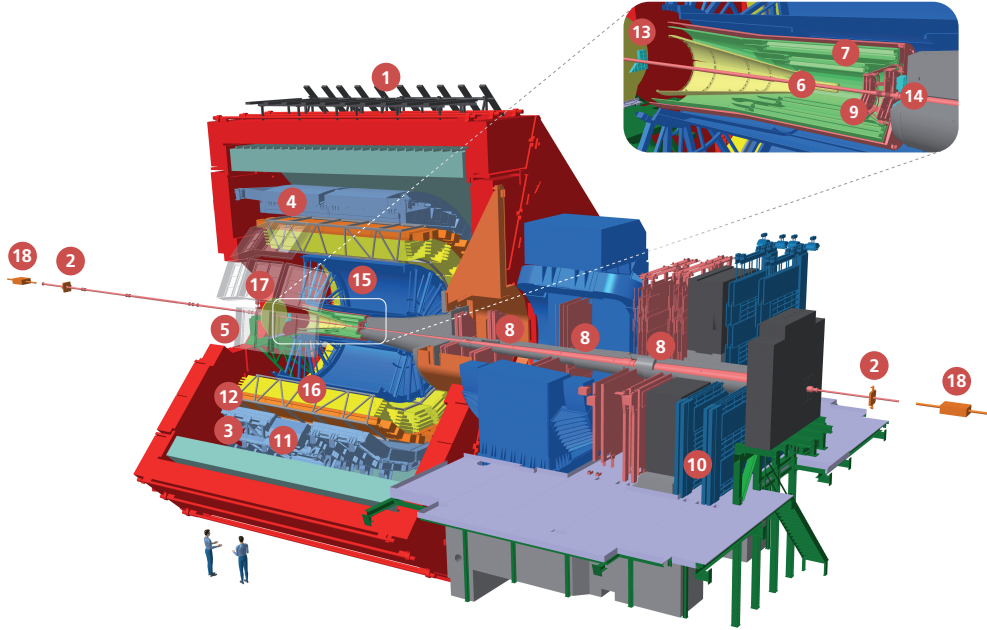

Figure 3.1 – Schematic overview of the LHC at CERN including ion beam energies at different stages of acceleration [18]

The data that is used in this thesis is gathered from a Pb-Pb run in november and december of 2018 in which lead ions were collided at an energy of $\sqrt{s_{\mathrm{NN}}} = 5.02$ TeV for each pair of colliding nuclei.

3.2   The ALICE detector

A Large Ion Collider Experiment or ALICE in short is one of the largest detector experiments at the LHC at CERN. It consists of 18 detector parts shown in the figure below. Its general purpose is to study the strongly interacting matter in heavy-ion collisions by measuring the mass, flight path, charge and energy of particles that pass through the detector elements. With this information of the particles that have been produced at the LHC collisions, the properties of the Quark Gluon Plasma can be studied more precisely. The strength of the ALICE detector lies in the fact that it can detect particles with lower p_T than other LHC detector experiments.
The detector itself weighs 10000 tonnes and has the dimensions of 26m long, 16m wide and 16m high and it lies more than 50 meters below the ground surface where it receives beams from the LHC. More than 1000 scientists and engineers from over 100 physics institutes contribute to this collaboration. [19]

Figure 3.2 – Schematic overview of the ALICE detector at CERN including its sub-detectors around the central beam pipe [**?**]

The following paragraphs describe the detector elements and data frames that are relevant for the analysis in this thesis.

3.2.1   ITS

The Inner Tracking System (ITS) is the detector element that is closest to the beam pipe. Its main purpose is to reconstruct the primary vertex and trajectories of the incoming particles with a total of six layers. From inside to outside, each in with 2 layers: Silicon Pixel Detectors (SPD) which have a very high spatial resolution , Silicon Drift Detectors (SDD) and Silicon Strip Detectors (SSD). The ITS covers the pseudorapidity region $|\eta| < 0.9$.[1] The ITS's dimensions run from 3.9 to 43 cm as seen from the beam pipe. Since the ITS is closest to the beam pipe and thus the interaction point of the collisions, it is vital in analysing particles with short decay times.

---

[1]Pseudorapidity is defined as $\eta = -\ln(\tan\frac{\theta}{2})$ with θ being the polar angle in the y-z plane which is the plane along the beam axis point straigt up and down

3.2.2 TPC

The Time Projection Chamber (TPC) is a cylindrical detector filled with gas placed around the ITS. It is used to identify and track particles traversing through the gas chamber. With its dimension from 84.1 to 246.6 cm from the beam pipe it also covers full azimuthal angle and pseudorapidity like the ITS. The gas in the chamber consists of mostly Argon and CO_2. Since charged particles can ionize the gas, the removed electrons can be attracted by strong electric fields from which the energy loss of the initial particles is calculated in readout chambers. A specific energy loss corresponds to a particle as illustrated in the following plot. The TPC is an important step in particle identification (PID).

ALI–PUB–92283
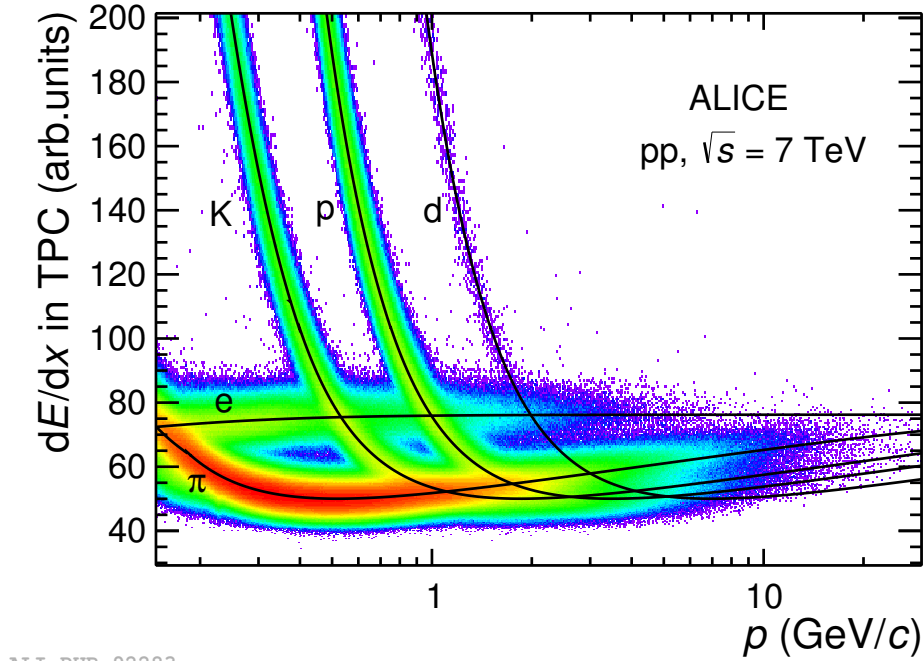
Figure 3.3 – Measured energy loss in the TPC for specific particles [13]

3.2.3 TOF

The Time Of Flight detector (TOF) uses the timed positioning of particles in the detector to identify them in the intermediate momentum range in the central region $|\eta| < 0.9$. Its dimensions are 377 to 399 cm from the beam pipe. It consists of a cylindrical array of Multigap Resistive Plate Chambers (MRPC) and strip detectors with an effective area of 141 m^2. The TOF also contributes to the identification of particles as can be seen in the following plot. [21]
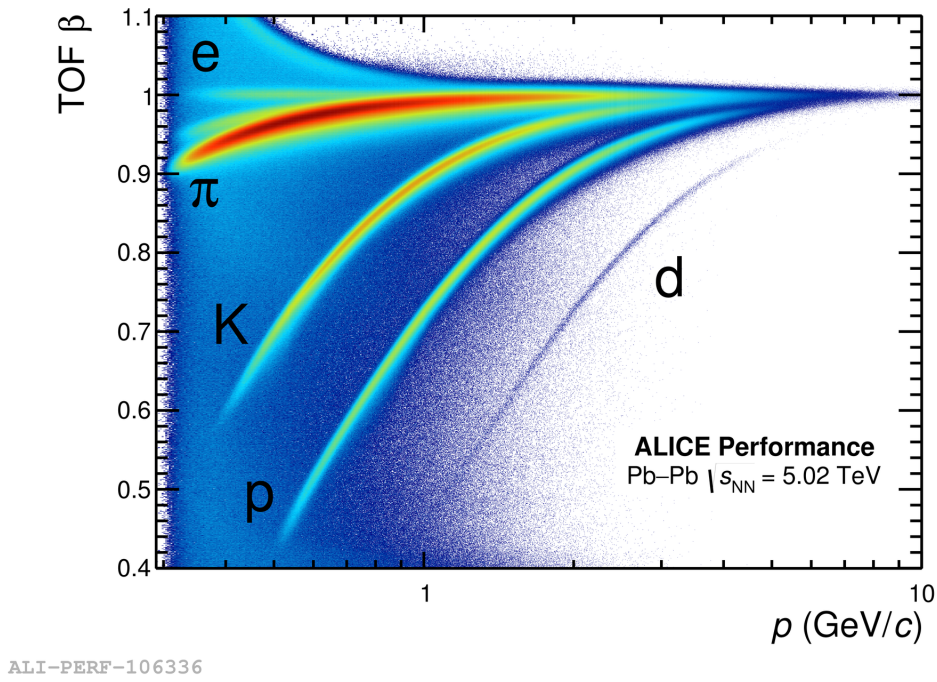
ALI−PERF−106336

Figure 3.4 – Time of Flight measurements for particle identification [13]

3.2.4   VZERO

The VZERO detector consists of two cylindrical units located at both sides of the interaction points at z = 328 cm and z = -86 cm. Each VZERO disc is made up of 4 concentric rings and is used for centrality determination and triggering. In this thesis, the kINT7 trigger is used on the data. This means that data is only taken from the other detectors when this signal is above this threshold in both the VZERO detectors. Also, the analysis is done only in the 60-80 % centrality regime
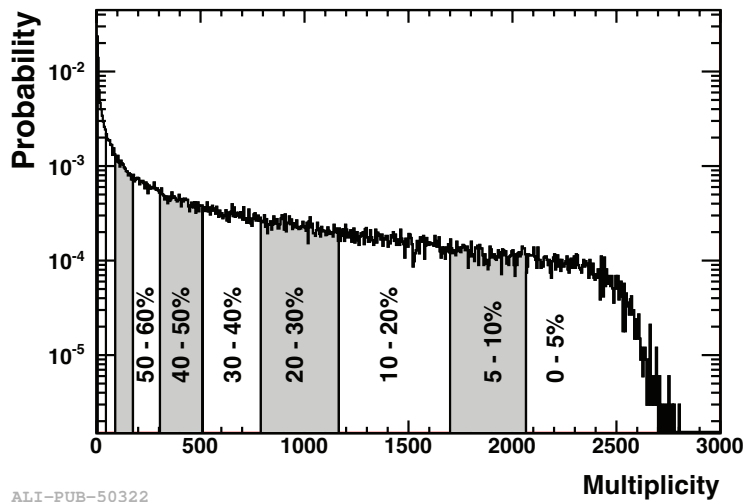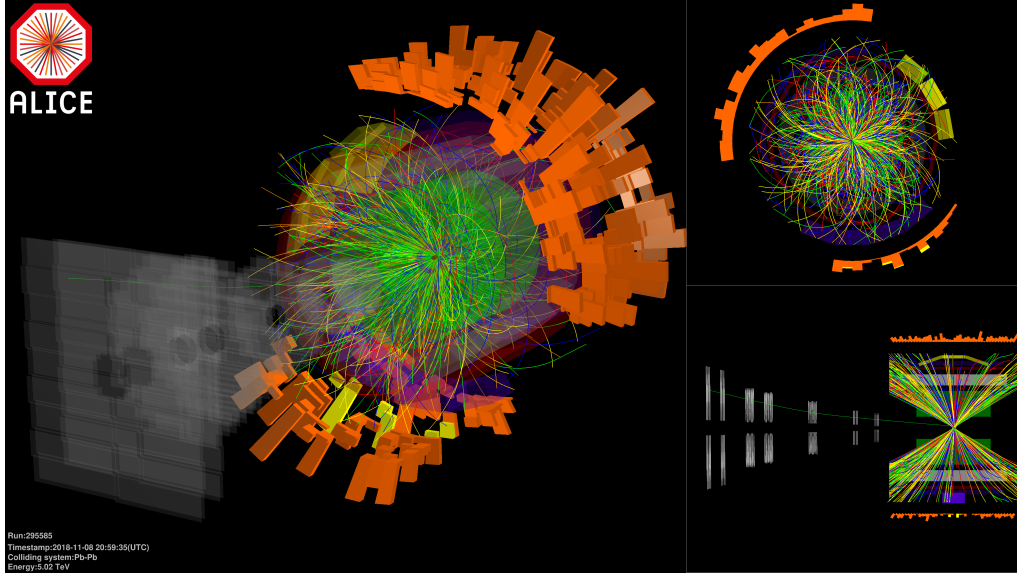

ALI−PUB−50322

Figure 3.5 – Probability as funciton of multiplicity in different centrality regions [13]

3.3   Alice data collection and workflow

As mentioned before, the data that was used in this thesis was collected in 2018 by the ALICE detector during the end of the year Pb-Pb run. An example of a collision is illustrated below.

Figure 3.6 – Collision of Pb ions at LHC with energy of 5.02 TeV per nucleon pair recorded by ALICE on 08 november 2018. The coloured lines represent the reconstructed trajectories of charged particles produced from the collision. [20]

The software package used for the offline[2] analysis of the ALICE data is called AliRoot. It is based on the ROOT [22] statistical analysis software which is a specialised C++ based framework built at CERN for data processing and analysing. Multiple AliRoot macros in the PWGHF/vertexingHF Github [23] are used in this thesis for the data analysis. In the vertexingHF directory, many macros are stored that are used to calculate the invariant mass distributions and make the cut files for the analysis.

AOD files are files that contain all the necessary information on the collisions that happen in the ALICE detector. Using the AliAnalysisTaskSEDStarSpectra.cxx task on the Grid, all events are analysed and only D^{*+} are stored for further analysis. Topological,track selections and PID are done with the AliRDHFDstartoKpipi class which generates cut files using a macro called makeTFileDstartoKpipi. With the macros FitMassSpectra and HFPtSpectrumRaa, raw yields and the nuclear modification factor can be calculated.

---

[2]Offline analysis is done after the data taking has taken place and online analysis is done in event selection and triggering the the ALICE detector itself

Chapter 4

D^{*+} yield measurement

4.1 Data used

The following sections will be on the datasets used for this thesis. Data was taken in November and December of 2018 during the Pb-Pb run of the LHC at CERN. During this short time of data taking, the ALICE detector received data in the Pb-Pb regime for the first time again since 2015. Hence the results in this thesis are also compared to the 2015 Pb-Pb run to ensure stability. Also, combining the results from 2015 and 2018 will provide smaller uncertainties. For the R_{AA} measurements, a p-p baseline is needed to do the calculations. This dataset is from the 2015 p-p run at the LHC at 5.02 TeV. The figure below shows the p_T differential production cross section for the D^{*+} in p-p collisions.
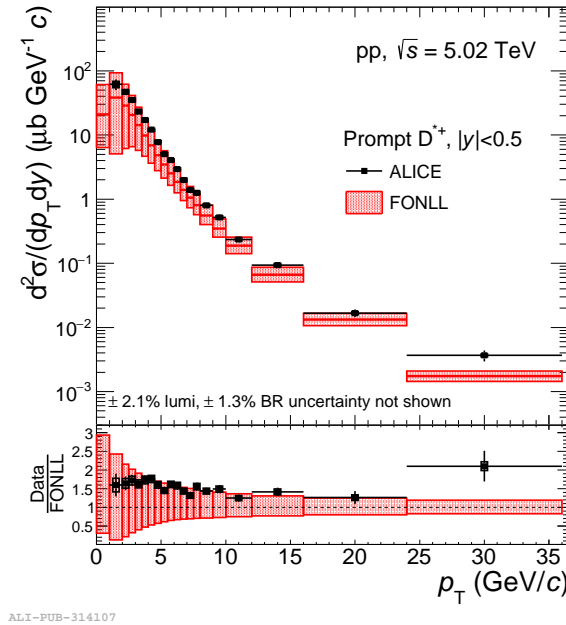
Figure 4.1 – p_T-differential production cross section of prompt D^{*+} in comparision with FONLL, in pp collisions at 5.02 TeV [13]

LEGO trains[24] were used and monitored using the MonALISA framework in this analysis. [25] The trains used for the analysis are: 1431 in the D2H PbPb for the raw yield extraction and 1257 in the D2H PbPb MC environment for the efficiencies.

Data gathered from the detectors is always compared to to Monte Carlo (MC) generated data. This is simulated data which contains all detector functionalities which are produced using the GEANT3 transport package[26]. It also contains physics processes as much as possible which are produced by the PYTHIA v6.421 generator.[27] Proper overlap between the Data and MC is therefore essential.. Before Data and MC samples are available to use by the ALICE collaboration, multiple investigations are done to ensure proper quality of the datasets. This is done by the DPG[28] and is discussed in the section on quality assurance.

4.1.1 Data sample

In this thesis, the minimum-bias Pb-Pb runs at $\sqrt{s_{\mathrm{NN}}} = 5.02$ TeV called LHC18q_pass1 and LHC18r_pass1 were used. The runlists connected to these runs that have been selected by the Data Preparation Group (DPG) are specified in Appendix A. These runs took place in November and December of 2018 and it includes 158 (83 in LHC18q_pass1 + 75 in LHC18r_pass1) million minimum bias events. The dataset has Aliphysics tag : AliPhysics v5-09-41d-01-1. The Pb-Pb sample that was analysed was recorded with a minimum bias trigger that requires that both V0 detectors have a signal in the scintillator arrays. Events that were reconstructed with a primary vertex that was approximately 10 centimeters from the centre of the ITS detector along the beam line were used. [29]. In this dataset, there are 23.4 million D^{*+} events as supposed to 20.0 million in the 2015 dataset.

4.1.2 Monte Carlo sample

The Monte Carlo (MC) generated data sample, LHC16i2c, is used as a reference to the data sample and to calculate efficiencies. The MC sample is not anchored to the data sample (LHC18q_pass1 and LHC18r_pass1) but is very similar in a way that it is anchored to the 2015 PbPb analysis that was used in previous D^{*+} analyses. By comparing the width and mean of the MC to the data sample and seeing sufficient agreement, the not anchored dataset can be used confidently. This can be seen in the figures below. Enrichment is applied to this MC sample, meaning that charm and beauty quark production is enhanced. The used run numbers are in Appendix B.
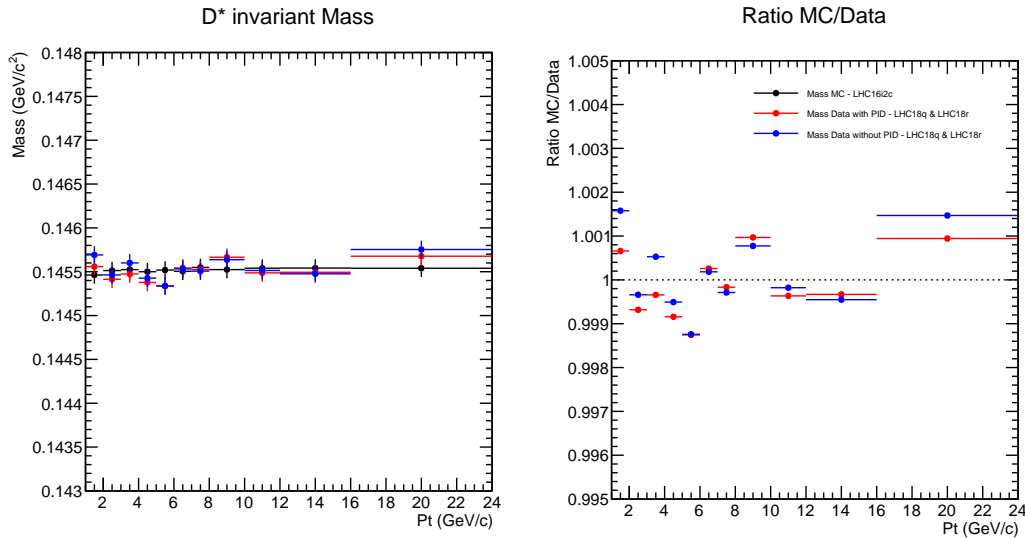
Figure 4.2 – Mass Comparison to MC data with and without PID
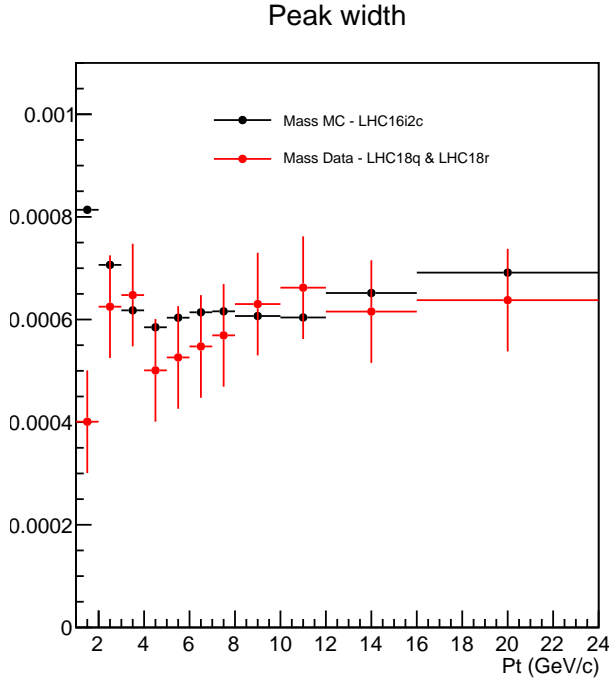
Figure 4.3 – Sigma (peak width) Comparison to MC data

4.1.3   Quality assurance of LHC18r & LHC18q

Before datasets LHC18r & LHC18q and their runlists are published for the ALICE collaboration to use, they are checked for quality by the DPG[28]. The detector responses for the TPC and TOF are analysed as can be seen in the following plot. For a full review of the quality assurance, see the QA talk. [30]

Figure 4.4 – Quality assurance of LHC18r & LHC18q dataset [13]

4.2 D^{*+} reconstruction

The reconstruction of the D^{*+} meson is done trough its hadronic decay channel: D^{*+} → D$^0\pi^+$ → K$^- \pi^+ \pi^+$ with branching ratios (67.7 ± 0.5 %) and (3.93 ± 0.04 %) respectively. [31] [32]. The mesons are reconstruc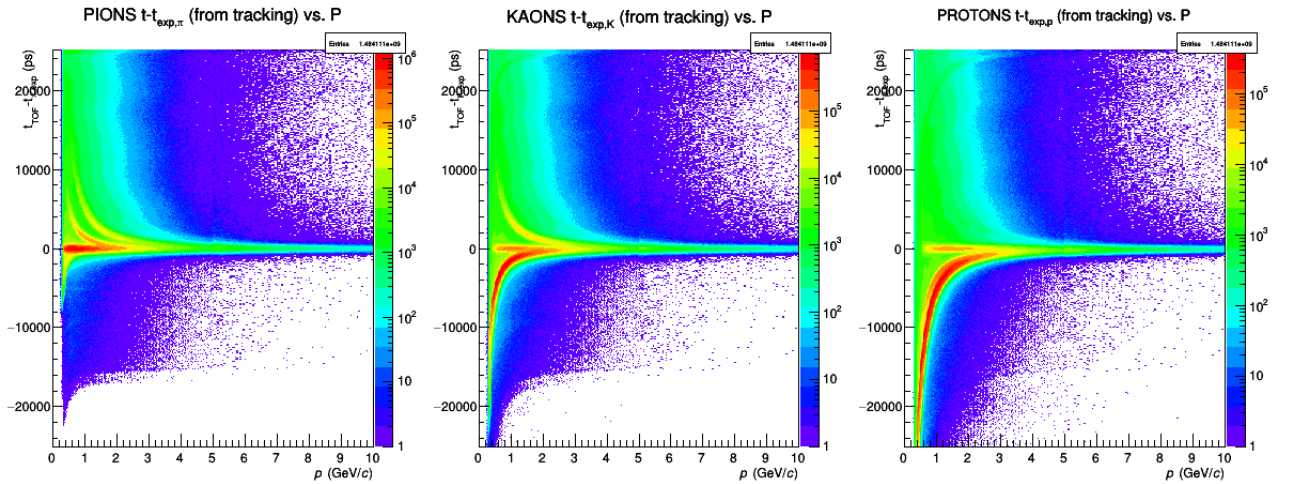ted in the central rapidity region. Since the decay of the D^{*+} meson happens through the strong decay, its primary vertex can not be reconstructed. Hence, the selections are applied to the daughter particle, D^0. Overall, the invariant mass distributions are taken from the decay topologies that are reconstructed with respect to the primary vertex.
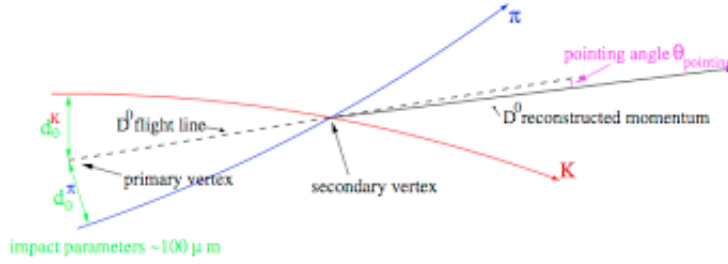

Figure 4.5 – Decay topology of the D^0 meson

4.2.1 Single Track Selections

Before the data is used in the analysis in the LEGO trains, selections take place in order to shorten CPU time on the GRID. There are requirements for the single tracks to have before they are taken into consideration for the analysis.

Firstly, secondary vertices of the D^0 mesons were only constructed using tracks that have $|\eta| < 0.8$ and $p_{\rm T} > 0.5$ GeV/c. These conditions are called the kITSrefit and KTPCrefit triggers. When these conditions are not met, the tracks are not stored. Secondly, in the TPC, there need to be a minimum of 70 rows that have signal but only if a cluster ratio of 0.8 was found. Thirdly, a cut on the impact parameter, the distance between the two colliding nuclei in the transverse plane, was put in place for tracks that have a transverse momentum less than 2 GeV/c. These particles have to have an impact parameter of at least 50 μm. Lastly, all tracks that have a soft π that comes from a D^{*+} meson, they have to have at least 70 out of 159 points in the TPC with a χ^2 less than 2. In addition, there has to be one signal in one of the SPD layers of the ITS that is corresponding to this track.

4.2.2 Topological selections

After a few single track selections, topological selections are made on the candidates in order to extract the D^{*+} signal. Based on the topology of the decay of the D^{*+} meson, or more specifically its daughter D^0, variables are chosen that can be used to reduce combinatorial background. The value of the cut that is applied can range significantly. The effect that the change in the topological selections has on the yield is discussed in section Selection Efficiency.

For this analysis, the cut values are mostly based on the values used in the 2015 Pb-Pb D^{*+} analysis. However, the cut values were revised by using the multi dimensional optimalisation approach. Using macros charmCutsOptimization and AddTaskSignificance from the vertexingHF Github[23], a correlation between the values of the cut variables and the significance can be optimised. Four variables have been chosen to investigate since they have proven to have the largest impact on the overall significance;

- Distance to closest approach (**DCA**) is the distance between the interaction point calculated from first estimating the primary vertex and the interaction point reconstructed from tracks of the K$^-$ and π^+.

- The product of impact parameters (**d0xd0**) is the distances between the backwards extrapolated tracks of the K$^-$ and π^+ towards the primary vertex and the primary vertex itself multiplied by each other.

- Cosine of the pointing angle(**cosThetaPoint**) is the angle between the flight line of the D^0, the line between the primary and secondary vertex and the reconstructed D^0 momentum measurement from the combined K$^-$ and π^+ tracks.

- The decay length (**NormDecayLengthXY**) is the distance over which the D^0 traverses before it decays.

This process was done for all p_{T} bins and the cut file was altered according to the highest significance in the multi-dimensional analysis. Below two examples of plots from the analysis followed by a table of reported D^{*+} significance before and after the alterations. The cut file was only changed with higher significance in the corresponding p_{T} bin. Also below is table of optimised cut values used in this thesis.

Significance wrt cosThetaPoint vs NormDecayLenghtXY (Ptbin0 1.0<pt<2.0)
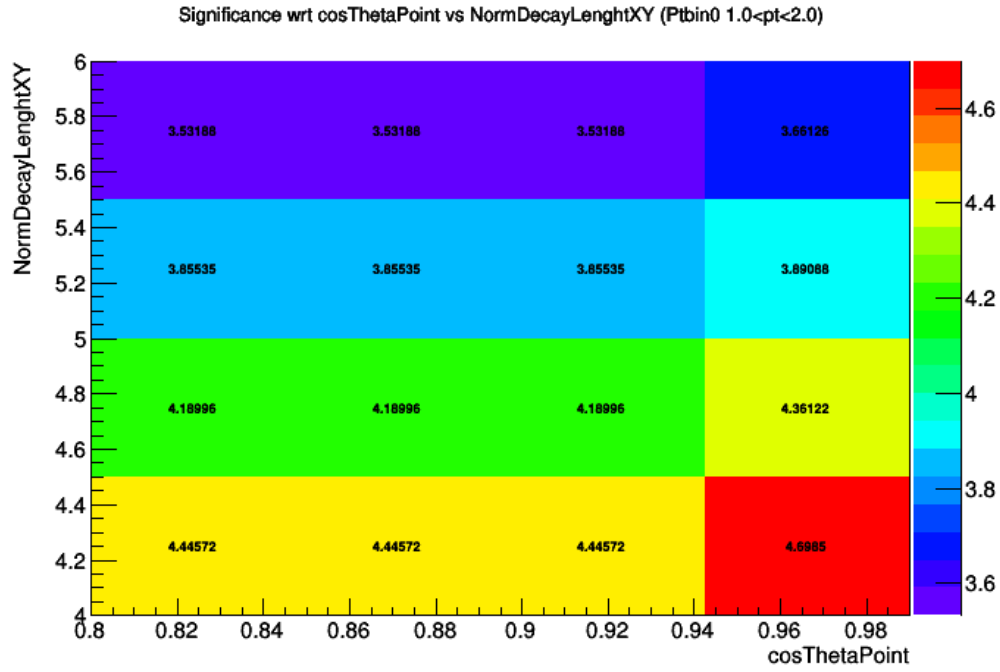
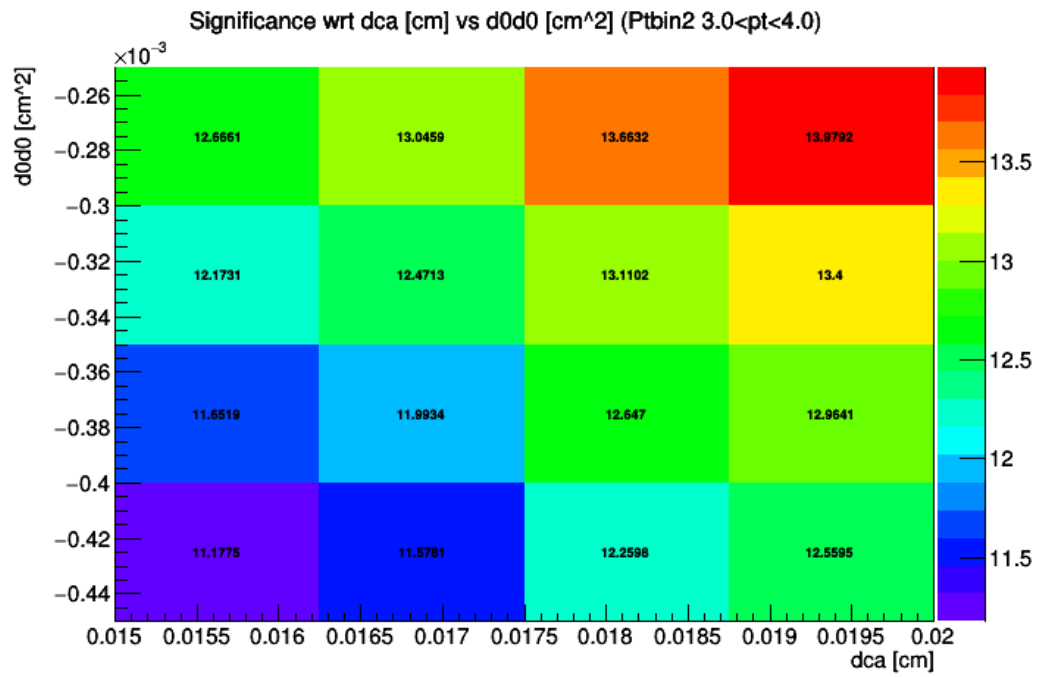**Figure 4.6** – Significance optimalisation for cosThetaPoint versus NormDecayLengthXY

Significance wrt dca [cm] vs d0d0 [cm^2] (Ptbin2 3.0<pt<4.0)

Figure 4.7 – Significance optimalisation for DCA versus d0xd0

	1-2	2-3	3-4	4-5	5-6	6-7	7-8	8-10	10-12	12-16	16-24
D0 inv [Gev/c]	0.023	0.027	0.032	0.032	0.04	0.045	0.055	0.06	0.074	0.10	0.10
DCA [cm]	0.025	0.023	0.02	0.022	0.023	0.023	0.02	0.022	0.02	0.06	0.06
Cos	0.8	0.8	0.8	0.8	1.0	1.0	1.0	1.0	1.0	0.9	0.9
Pion pt [GeV/c]	0.8	0.85	0.9	1.0	1.0	1.0	0.9	0.9	0.7	0.5	0.5
Kaon pt [GeV/c]	0.8	0.85	1.0	1.0	1.0	1.0	0.9	0.9	0.7	0.5	0.5
d0 Kaon [cm]	0.1	0.1	0.1	0.1	0.08	0.1	0.12	0.15	0.15	0.1	0.1
d0 Pion [cm]	0.1	0.1	0.1	0.1	0.08	0.1	0.12	0.15	0.15	0.1	0.1
d0xd0 [cm2]	-0.00040	-0.00018	-0.00025	-0.0002	-0.00023	-0.00007	-0.000055	-2.e-05	2.5e-05	0.0001	0.0001
Cosine Pointing Angle	0.8	0.90	0.9	0.9	0.93	0.85	0.95	0.85	0.85	0.7	0.7
D* Inv Mass half width	0.3	0.3	0.3	0.2	0.3	0.3	0.3	0.3	0.3	0.15	0.15
Half width	0.15	0.15	0.15	0.15	0.3	0.15	0.15	0.15	0.15	0.03	0.03
Pt min of Pi soft [GeV/c]	0.05	0.05	0.05	0.05	0.25	0.3	0.3	0.3	0.3	0.1	0.1
Pt max of Pi soft [GeV/c]	0.5	0.5	0.5	10.	10	100	100	100	100	100.	100.
theta angle between [rad]	0.5	0.5	0.5	0.5	0.5	0.5	0.5	1.	1.	9999.	9999.
cosThetaPointXY	0.7	0.7	0.7	0.7	0.7	0.7	0.7	0.7	0.7	0.8	0.8
NormDecayLenghtXY	4.0	5.0	4.0	4.5	4.0	3.0	2.0	0	0.	0.	0.

Figure 4.8 – Topological selections as applied in the D*+ meson decay analysis

4.2.3 Particle Identification

As mentioned before, the TPC and TOF detector elements are used for particle identification that helps reconstructing D*+ mesons by identifying pions and kaons that arise from the decay process. The identification of these particles help to differentiate background from signal, especially in the low momentum region.

A 3σ compatibility between the expected and measured signals in the TPC for dE/dx and time of flight in the TOF were applied to the D*+ candidate daughters that are kaons and pions. However, when there was no TOF signal, only the TPC signal was used in the analysis. The PID strategy reduces the background significantly except for higher p_T bins 12-16 and 16-24 GeV/c the PID does not reach the desired effect of raising the significance. Hence PID is not used for the higher p_T bins. For an analysis of the uncertainties involved with the PID (PreSelect fucntion in cut object), the section Systematic Uncertainties elaborates further.

4.2.4 Signal extraction

The raw signal for the D*+ meson is obtained through calculating the invariant mass distribution of the mass difference $\Delta M = M (K\pi\pi) - M(K\pi)$. The signal is fitted with a Gaussian, the background is fitted with a threshold function convoluted with a power law as follows with x being the invariant mass:

$$f_{background} = a\sqrt{x - m_\pi}e^{b(x-m_\pi)} \qquad (4.2.1)$$

The invariant mass distributions are reported in the following figures, each with p_T range from 1 to 24 GeV/c. As can be seen, significances range from 3.5 σ to 9.1 σ. These plots are used to see if the fits are done correctly throughout all p_T ranges.
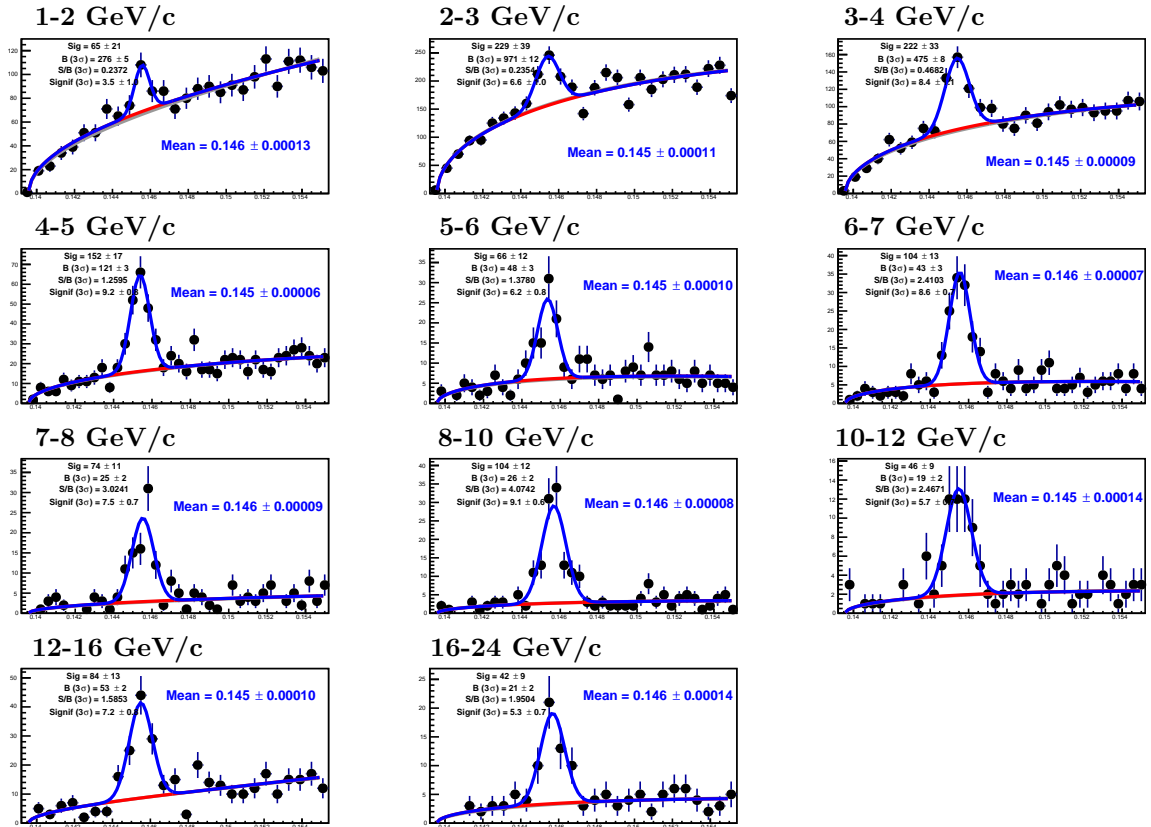

Figure 4.9 – Mass spectra of invariant mass (K$\pi\pi$ - Kπ) of D*+ in different transverse momentum bins. The blue line is signal and background in red.

Figure 4.10 – Mass spectra of invariant mass (Kππ - Kπ) for true MC only of D∗+ in different transverse momentum bins. The blue line is signal and background in red.

The width of the peaks in the MC data sample are used to fix the widths of the mass spectra from data.

Figure 4.11 – Mass spectra of invariant mass (Kππ - Kπ) of D∗+ in different transverse momentum bins. The blue line is signal and background in red.

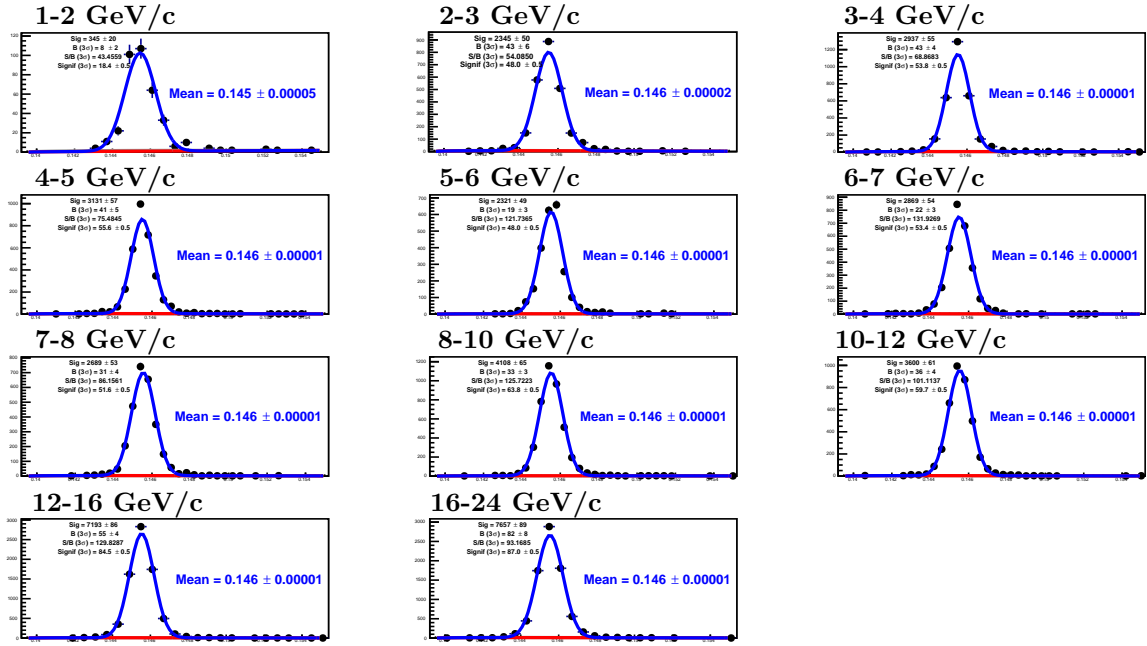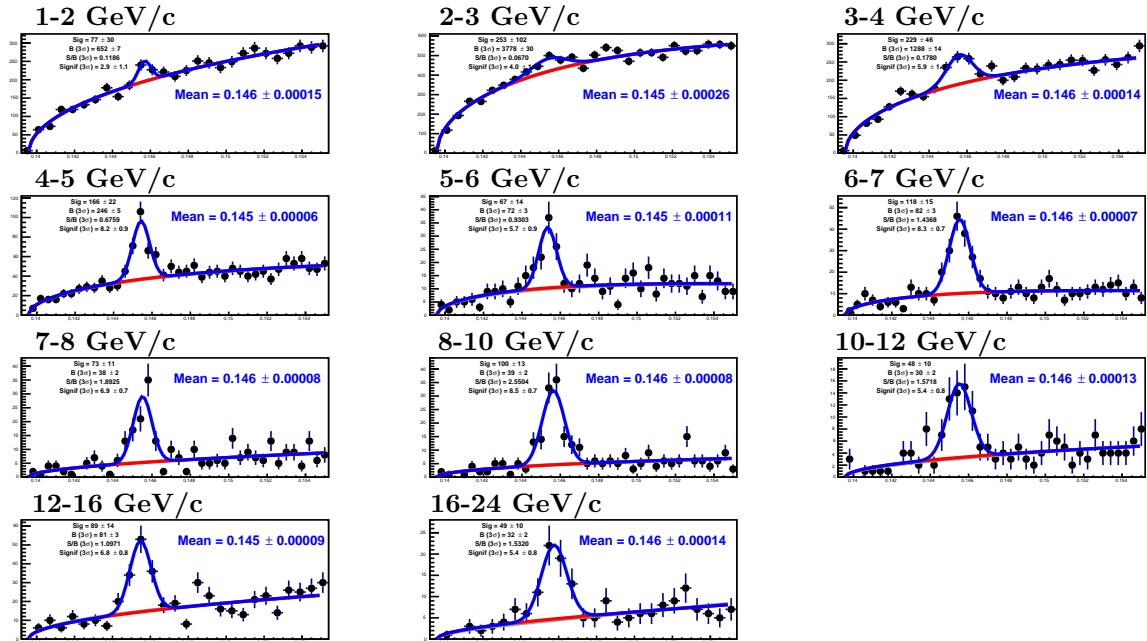In the higher p_T bins, 12-16 GeV/c and 16-24 GeV/c, the PID is not accurate since the different particle lines in the TPC (dE/dx) and TOF (time of flight) overlap. The following table shows the raw yield, signal/background and significance obtained from the mass spectra.

|	Raw Yield	Signal/Background	Signifcance
1-2	65 $\pm$ 21	0.2372	3.5 $\pm$ 1.0
2-3	229 $\pm$ 39	0.2354	6.6 $\pm$ 1.0
3-4	222 $\pm$3 3	0.4682	8.4 $\pm$ 1.1
4-5	152 $\pm$ 17	1.2595	9.2 $\pm$ 0.8
5-6	66 $\pm$ 12	1.3780	6.2 $\pm$ 0.8
6-7	104 $\pm$ 13	2.4103	8.6 $\pm$ 0.7
7-8	74 $\pm$ 11	3.0241	7.5 $\pm$ 0.7
8-10	104 $\pm$ 12	4.0742	9.1 $\pm$ 0.6
10-12	46 $\pm$ 9	2.4671	5.7 $\pm$ 0.7
12-16	84 $\pm$ 13	1.5853	7.2 $\pm$ 0.8
16-24	42 $\pm$ 9	1.9504	5.3 $\pm$ 0.7

4.2.5   Acceptance x Efficiency

In order to calculate the differential yield of the D^{*+}, the raw yield is only one of the needed pieces of the puzzle. The detector Acceptance x Efficiency and the relative B meson feed down contributions also have to be calculated. According to the following equation, the prompt D^{*+} yield is calculated. This is done with the LHC16i2c MC dataset.

$$\frac{dD^{*+}}{dp_{\mathrm{T}}} = \frac{1}{2}\frac{1}{\Delta y \Delta p_{\mathrm{T}}}\frac{f_{prompt}(p_{\mathrm{T}}) \cdot N_{raw}}{(Acc \times \epsilon) \cdot BR \cdot N_{evt}} \tag{4.2.2}$$

The detector acceptance is defined as the geometrical limits of the detector where the efficiency is the the accuracy with which the detector can measure a signal or background event.

At low p_{T} the (Acc x ϵ) is lower due to the lower resolution of the detector and tighter cuts that are applied in the analysis. Also at low p_{T}, the bottom efficiency is higher than the charm efficiency because of its longer lifetime thus more accurate tracking.

At high p_{T}, the efficiency overall is higher due to looser cuts. Also, the different efficiencies for prompt and feed down become similar at high p_{T}.
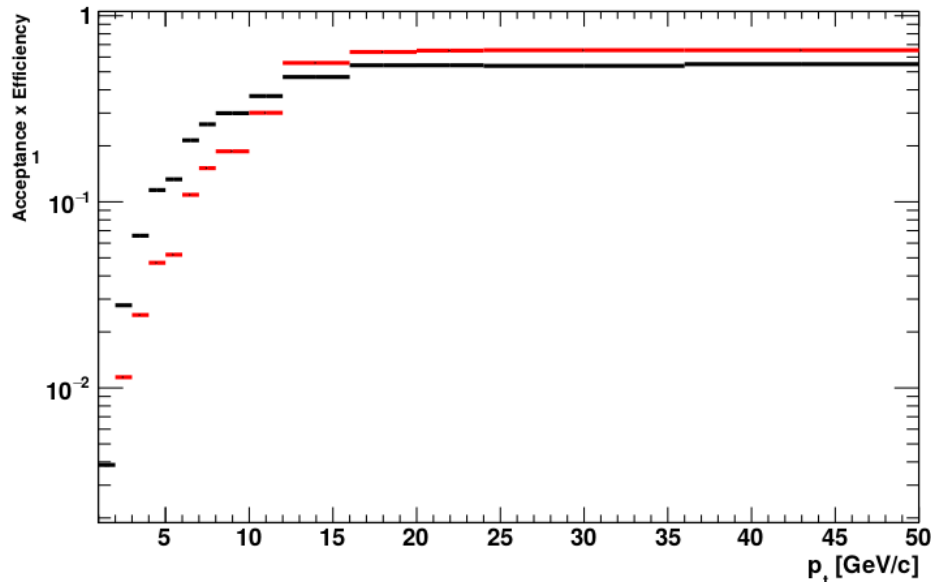
Figure 4.12 – Efficiencies from promt en feed down as function of p_{T}. Prompt (charm) in red and B-feed down (bottom) in black

4.3 Systematic uncertainties

Before the results can be shown, all the systematic uncertainties have to be assigned. In this analysis of the D^{*+} R_{AA} there are multiple sources of uncertainties namely:

- Uncertainty due to Raw Yield extraction from invariant mass distributions

- Uncertainty from Cut variations

- Uncertainty from Particle Identification (PID)

- Uncertainty due to MC p_T shape from simulation

- Uncertainty due to pile-up

- Uncertainty due to feed down subtractions

The following sections will evaluate all these factors of uncertainties in detail.

4.3.1 Raw Yield

To assign systematic uncertainties to the yield extraction, a multi trial yield extraction technique is applied. This entails the following:
For a single invariant mass fit bin, multiple different techniques are used to extract the raw signal.

1. Varying the amount of bins

2. Vary the fit interval to 0.160 GeV/c^2

3. Vary the fit interval to 0.165 GeV/c^2

4. Vary the background function used in the fit.

For a single invariant mass fit, each mass bin is smeared according poissonian statistics 10800 times in order to obtain 10800 independent mass fits starting from the original. Then, all points enumerated above are applied in bunches of 2200 mass plots. All this is done while there is a quality criterium applied of the width of the peak being within 2 σ of the MC width of the peak. Then, the resulting signal is plotted in a histogram. This histogram is fitted with a Gaussian to calculate the variation on with respect to the single trial fit.

The resulting plot shows the variations in the signal in the top left, sigma in the top right, mass in the bottom left and the filled histograms in the bottom left. The different colours are the different fit variations. As can be seen, no large deviations can be seen from the variations which means that the fitting procedure used is stable. For all the p_T bins used in this analysis, the RMS is calculated from the histograms and the uncertainty is assigned.
As can be seen in the table below, the main source of uncertainty in this procedure is fitting an alternate background. This is due to the fit with a linear background that is also tried. However, this is not a realistic background shape.

p_{T}	Std mean	Rebin	160	165	Alt Bck
1-2	84	82	83	81	84
2-3	230	260	224	221	221
3-4	223	239	228	223	208
4-5	160	162	161	161	152
5-6	67	71	67	67	68
6-7	104	106	103	105	104
7-8	75	75	76	76	75
8-10	47	48	49	49	47
10-12	47	49	48	49	49
12-16	84	82	83	83	88
16-24	43	44	42	43	43
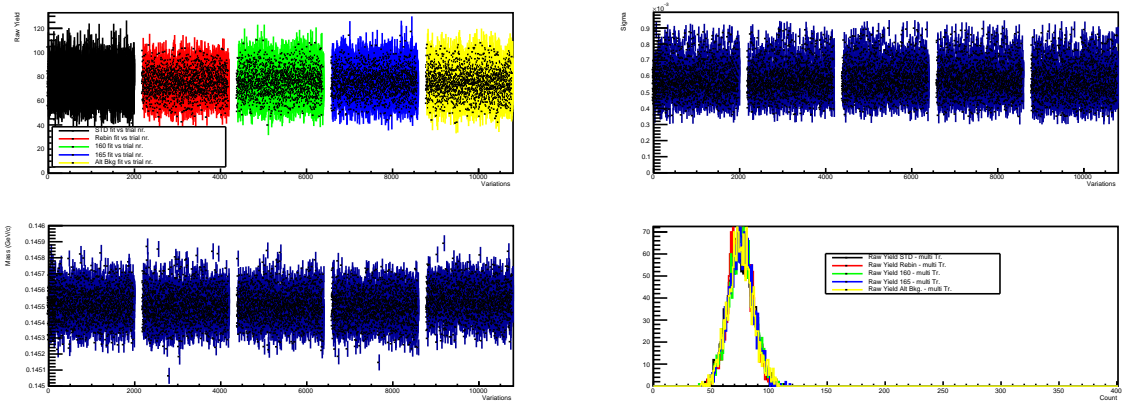
Figure 4.13 – Investigating the errors on raw yield in the 7-8 GeV/c p_{T} bin with multi-trial fit approach

4.3.2 Cut variations

To ensure stability of the fit, variations on the cut values as described earlier are applied. When altering the cuts 5,10,15 or 20%, the corrected yield should still be stable under these variations to ensure a stable fit. A large deviation in corrected yield while varying the cut values means that the cut values have to be chosen differently.

First, the raw yield and efficiency are calculated with the variations in Distance to closest approach (DCA), product of kaon and pion impact parameters (d0xd0), angle between the D^0 flight line and the reconstructed D^0 (CosThetaAngle)[1] and length of decay of the D^0 (Normalised Decay). It is expected that the raw yield and efficiency both very a significant amount under cut variations. However, when the corrected yield which is calculated from these two values is stable, the end result is stable under cut variations.

---

[1]For the CosThetaAngle, the difference with the value of 1 is varied in percentages.
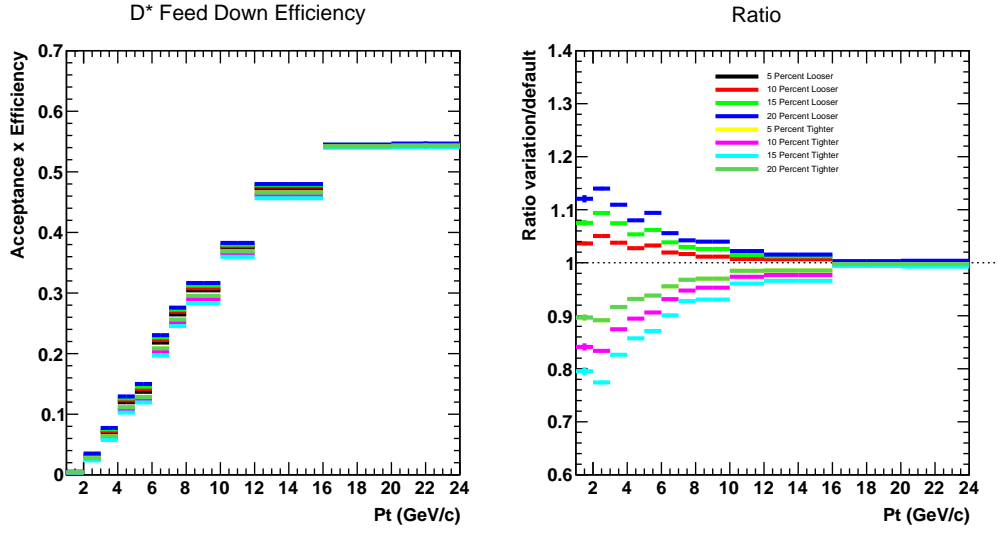
Figure 4.14 – Effect of Cut Variations on Efficiencies

As can be seen in the figure above, the efficiency varies a lot due to cut variations. There is also an ordering in the percentages of cut variations with larger variations in cut resulting in a larger difference in Efficiency.
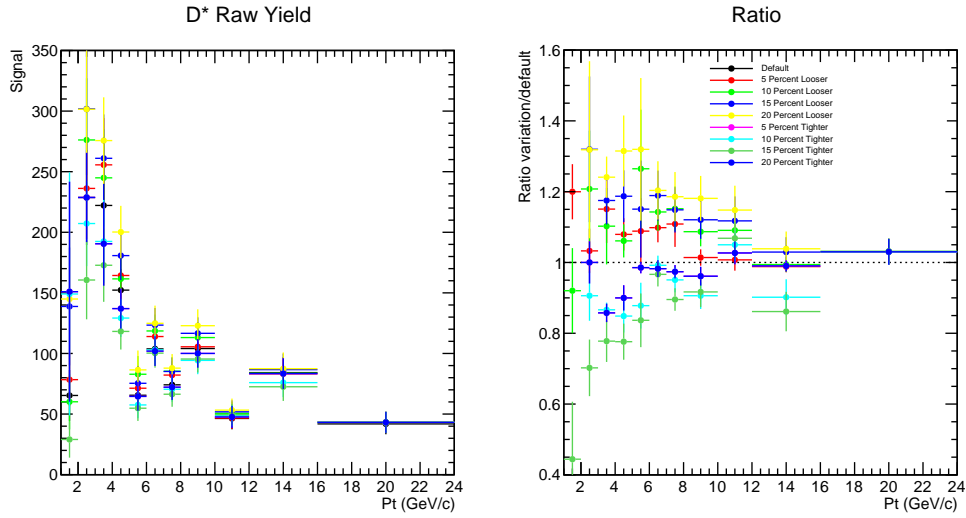

Figure 4.15 – Effect of Cut Variations on Raw Yield

In the plot below, the effect of cut variations on the corrected yield can be seen. The corrected yield varies only slightly from cut variations which shows that the corrected yield is stable under variations of the cut values used in the D^{*+} extraction.
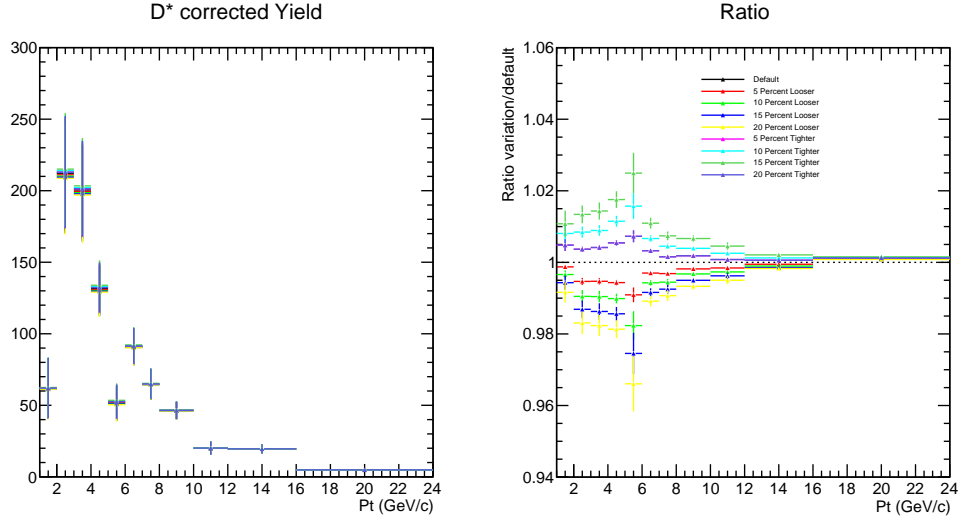
Figure 4.16 – Effect on corrected yield from cut variations

p_T	1-2	2-3	3-4	4-5	5-6	6-7	7-8	8-10	10-12	12-16	16-24
Cut variation	1%	1%	1%	1%	2%	1%	1%	1%	1%	0%	0%

4.3.3 PID

To study the effect of Particle Identification (PID) on the end result, the raw signal with and without PID is calculated separately. As can be seen in the following plot, there is no significant difference within uncertainties between the two. The horizontal line is fitted with a function that has an average of 1.01232 ± 0.0259586. Hence, no systematic uncertainty is assigned to the PID strategy.
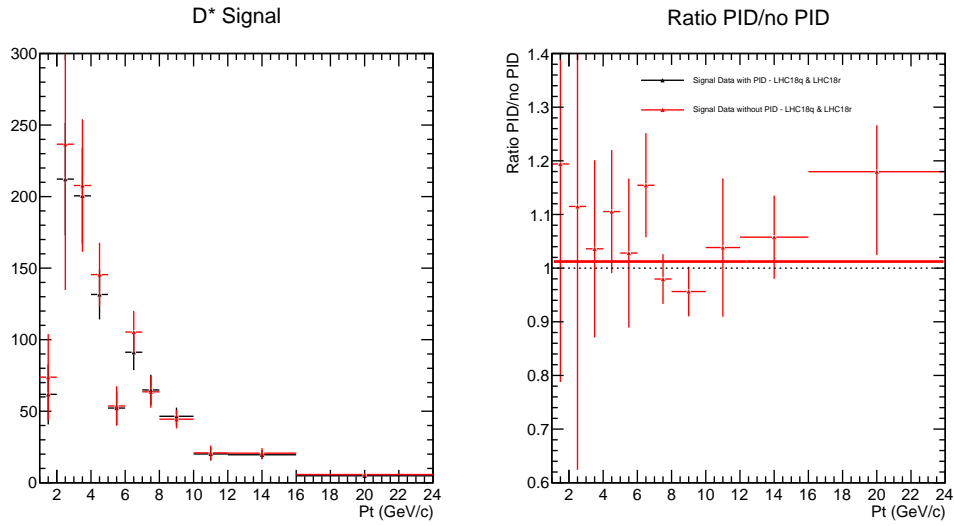

Figure 4.17 – Efficiencies Cut Variations

4.3.4 MC p_T shape

The shape of the transverse momentum distribution in MC and data have to be compared in order to rule out any bias. Hence, the MC p_T shape is calculated with different weights in order to investigate the effect of the weights on the p_T shape. FONLL [33] and FONLL+BAMPS[34] weights are compared to check stability for both Charm and Bottom efficiencies. This is done by using the AliCFTaskVertexingHF on the GRID On the right, the ratio between the two weights is plotted to assign the systematic uncertainties. Only in the lower p_T region there is a significant difference between the two weights.
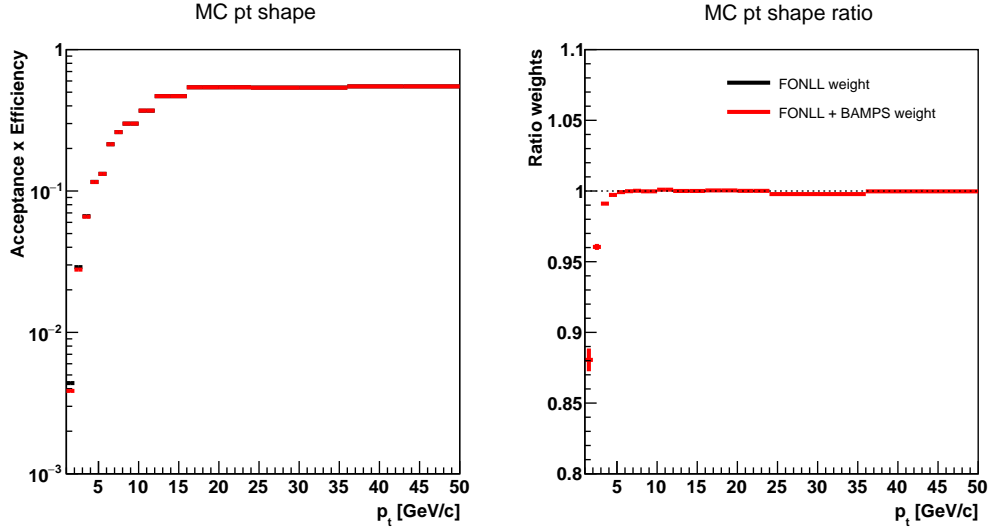
Figure 4.18 – Efficiencise with FONLL or FONLL BAMPS including the ratio for b quarks
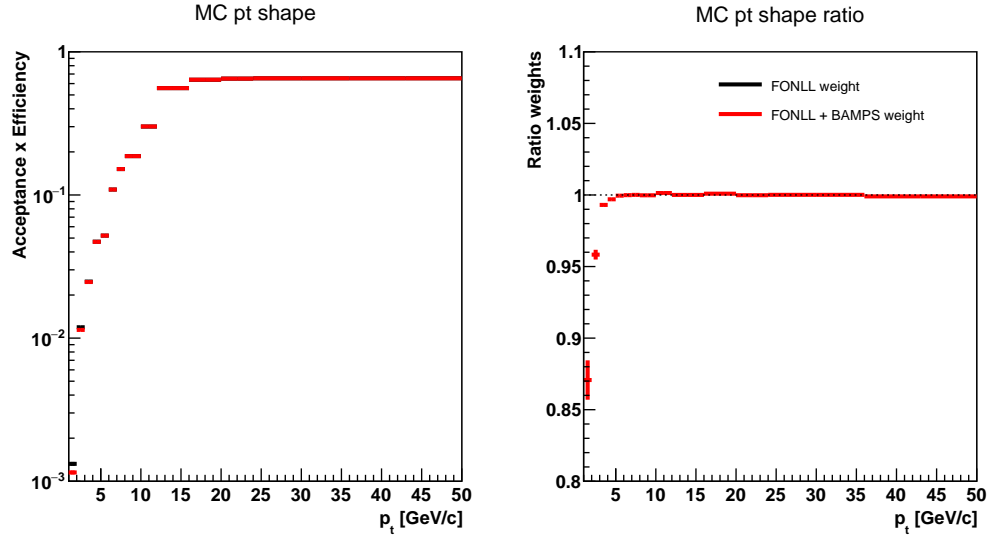
Figure 4.19 – Efficiencise with FONLL or FONLL BAMPS including the ratio for c quarks

p_T	1-2	2-3	3-4	4-5	5-6	6-7	7-8	8-10	10-12	12-16	16-24
Uncertainty	12%	4%	1%	0%	0%	0%	0%	0%	0%	0%	0%

4.3.5 Pile-up

Pile up is when there are there are multiple simultaneous interactions per bunch crossing. The probability for pile up events in the dataset used is negligible. Below a figure is shown that compares the D^0 mass and sigma for pile up and non pile up corrections. As can be seen, they are within uncertainties the same. There is no systematic uncertainty assigned to pile-up events. [35]
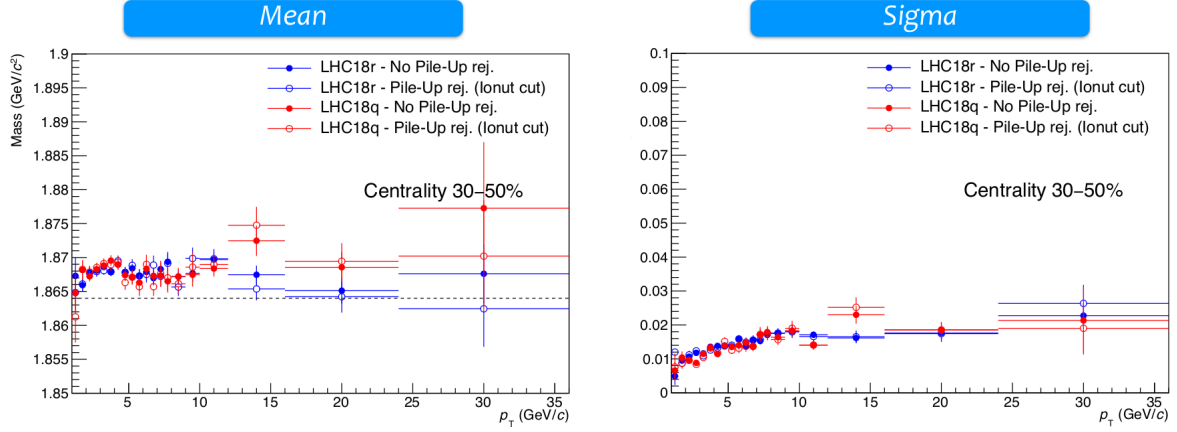

Figure 4.20 – Pile up quality assurance [13]

4.3.6 Feed-Down subtraction

Since D^0 mesons can also be produced from the decay of a B-meson, there has to be a correction for the second source of D^0 in order to calculate the prompt yield. The factor f_{prompt} which is the factor that specifies the amount of D^0 mesons from the c quark, has been calculated using the cross section from FONLL calculations according the the following formula:

$$f_{prompt} = 1 - \frac{N_{raw}^{Dfeed-down}}{N_{raw}^D}$$

$$= 1 - \langle T_{AA} \rangle \cdot (\frac{d^2\sigma}{dy dp_T})^{FONLL} \cdot R_{AA}^{Feed-down} \cdot \frac{\Delta p_T (Accx\epsilon)_{feed-down} \cdot BR \cdot N_{events}}{\frac{1}{2} N_{raw}^D}$$

Where $N_{raw}^{Dfeed-down}$ is the estimated raw yield of D mesons from B hadron decays, N_{raw} is the measured raw yield in this analysis. $\langle T_{AA} \rangle$ is the average nuclear overlap function, $(\frac{d^2\sigma}{dy dp_T})^{FONLL}$ is the production cross section from B mesons in FONLL. The factor is normalised using the (Acc x ϵ), Branching ratio (BR) amount of events (N_{evt}).

| p_T	1-2	2-3	3-4	4-5	5-6	6-7	7-8	8-10	10-12	12-16	16-24
Uncertainty upper	5%	5%	7%	7%	8%	7%	7%	7%	5%	3%	3%
Uncertainty lower	5%	5%	7%	7%	9%	8%	8%	7%	5%	3%	3%
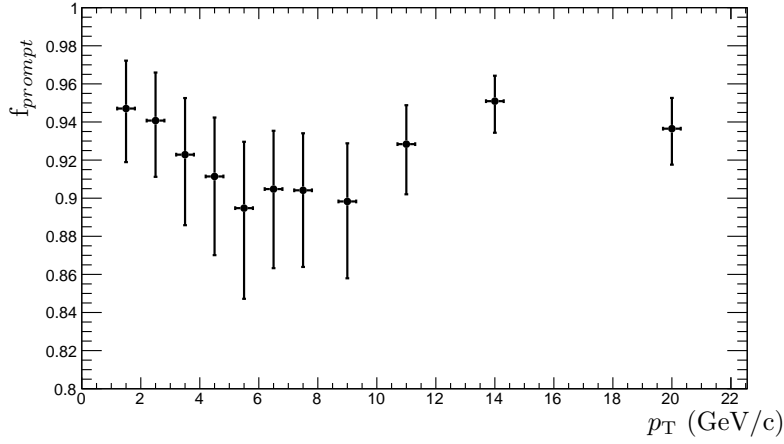
The uncertainty is calculated from using two different methods to calculate the R_AA namely the fc and nb method. The fc method is based on the ratio of charm to beauty and the nb method is based on the beauty cross section. The uncertainties for both these methods have a certain uncertainty band. When they are convoluted, this results in an upper and lower uncertainty as can be seen in the following plot and table.

p_T	1-2	2-3	3-4	4-5	5-6	6-7	7-8	8-10	10-12	12-16	16-24
Cut variation	1%	1%	1%	1%	2%	1%	1%	1%	1%	0%	0%
Raw Yield	2%	7%	5%	3%	3%	1%	1%	3%	4%	3%	2%
PID	0%	0%	0%	0%	0%	0%	0%	0%	0%	0%	0%
p_T Shape	12%	4%	1%	0%	0%	0%	0%	0%	0%	0%	0%
B-Feed down	5%	5%	7%	7%	9%	8%	7%	7%	5%	3%	3%

4.4 Uncertainties summarised

In the figure below, all sources of uncertainty are shown together in the same plot. Overall, all systematic errors are around 15% which is within reasonable amounts for this analysis. Also, a table is shown with all the individual uncertainties that have been calculated in this chapter.
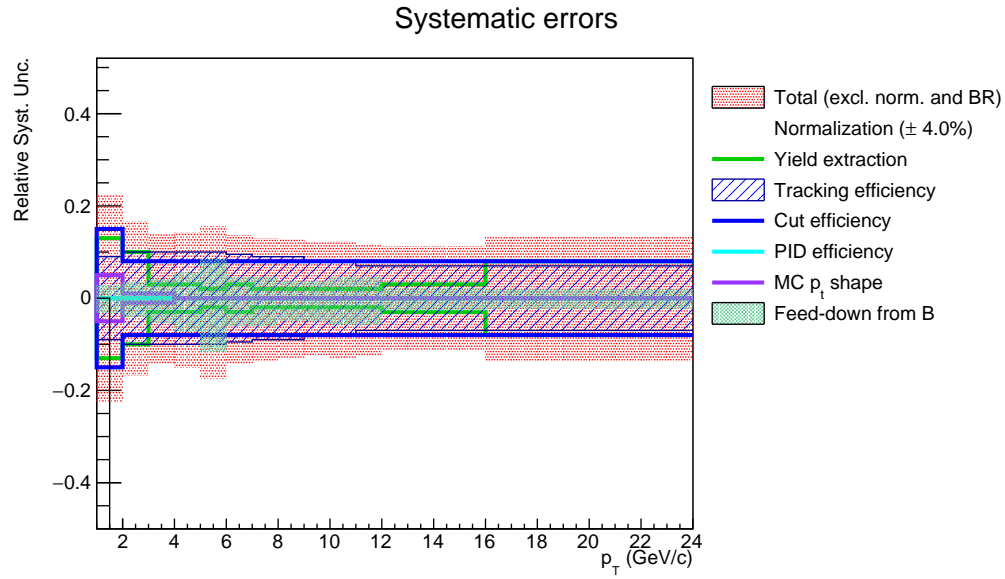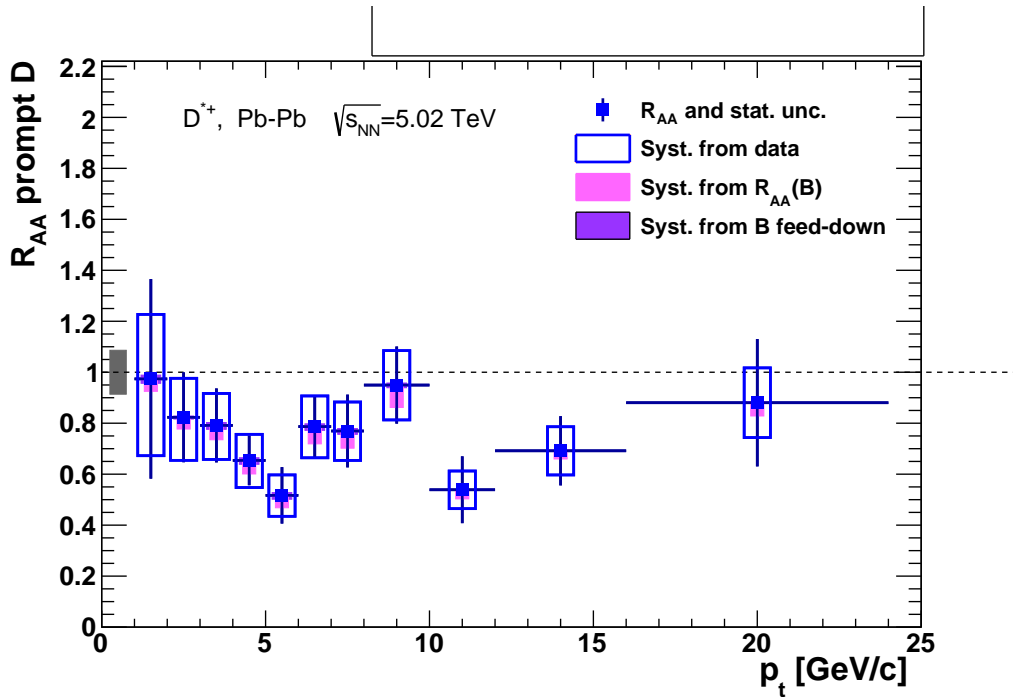

Figure 4.21 – Overview of uncertainties

Chapter 5

R_{AA} measurement

5.1 Nuclear Modification Factor

Figure 5.1 – Nuclear Modification Factor R_{AA} as function of transverse momentum p_T

In the figure above, the calculated R_{AA} can be seen. The blue boxes indicate the systematic uncertainty from data, the pink box gives the systematic uncertainty from the R_{AA} calculation and in blue the systematic uncertainty from feed-down subtractions are shown. The average R_{AA} in the 60-80% centrality shows a suppression of about 20% with some p_T dependence. However, the uncertainties are still too high to have any strong conclusions on the suppression of the R_{AA} in all p_T bins, especially in the lower p_T bins.

Since the 2015 R_{AA} measurement is in the same centrality class and with the same centre of mass energy, both datasets can be combined. Below is the plot with the results from the 2015 analysis together with the values found in the analysis in this thesis. The systematic and statistical uncertainties are weighted for the average of the two as can be seen in green.
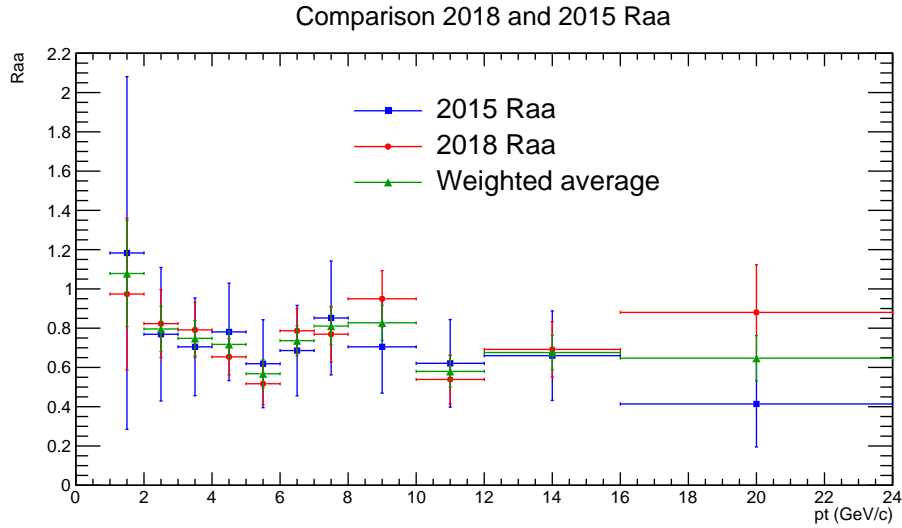
Figure 5.2 – Results from 2015 and 2018 R_{AA} measurement including the weighted average

The combining of the two datasets provides two times as much data, and in turn two times less systematic and statistic uncertainties. For comparison with the different centrality classes 0-10% and 30-50%, the weighed average is used as can be seen in the following plot.
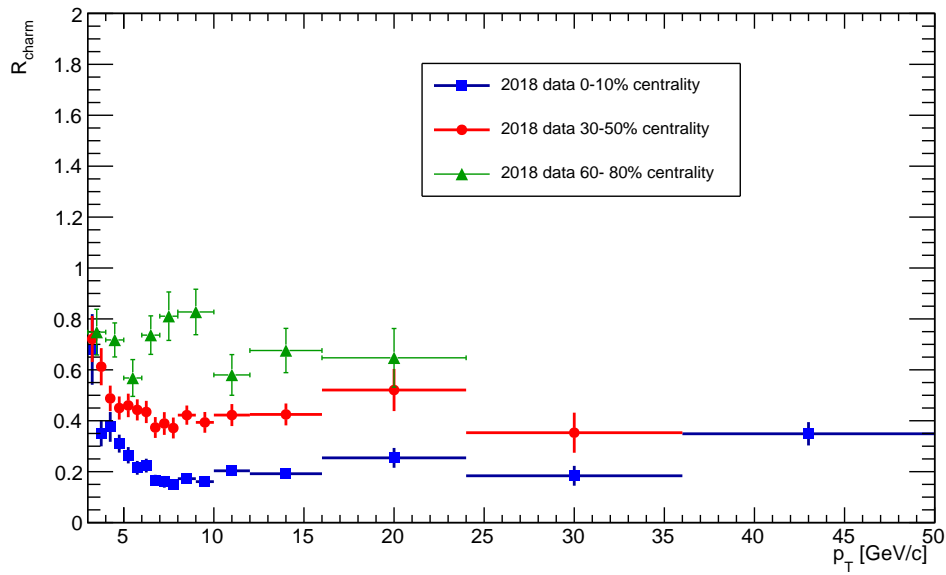

Figure 5.3 – Comparison with different centrality bins in 2018 data

There seems to be a hint of ordering in the centralities, with the more central collisions producing a lower R_{AA}. For more central collisions, more events take place hence the p_T range can be extended to higher than 24 GeV/c.
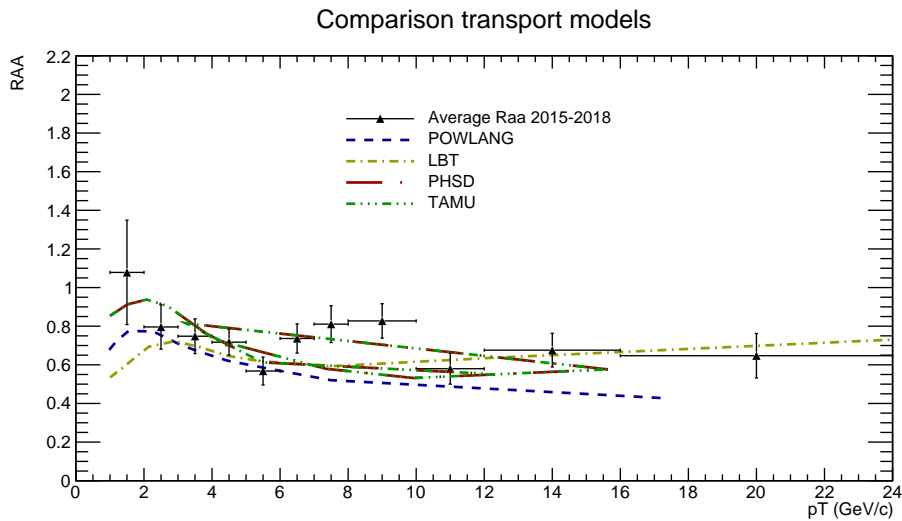
5.2 Comparison with theoretical models

As a reference for the result, the calculated R_{AA} is compared to theoretical models. Theoreticians have calculated the R_{AA} using models with different energy transfer models. As can be seen in the plot below, the R_{AA} calculated in this thesis is compatible within uncertainties with pQCD models. Djordjevic[36] and CUJET3.0[37] include both radiative and collisional energy loss processes, SCET[38] implements medium-induced gluon radiation. The SCET model however, seems to report values higher than the values reported in this thesis. The uncertainties in the reported R_{AA} in this thesis are not small enough to differentiate between the theoretical models.
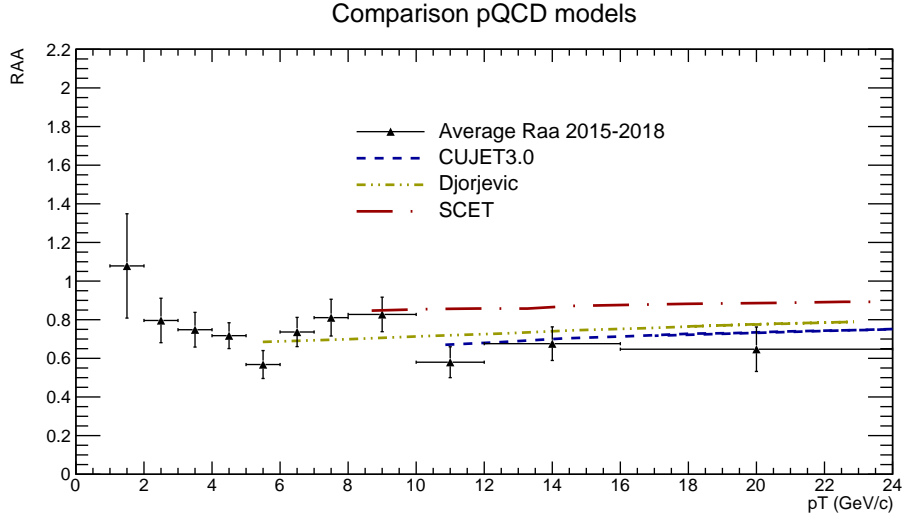
Figure 5.4 – R_{AA} comparison with theoretical models based on pQCD energy loss. Uncertainties are systematic and statistical added up.

The same comparison is made with a different set of models based on transport. For POWLANG [39] and TAMU [40], interactions are described by collisional processes. For LBT [41] and PHSD[42] the energy loss comes from medium-induced gluon radiation and collisional processes. As can be seen in the plot below, the models seem to describe the data points troughout the whole p_T range except for the POWLANG model.

Figure 5.5 – R_{AA} comparison with theoretical models based on transport models. Uncertainties are systematic and statistical added up.

Overall, the data points seem to be described by theory reasonably well. The data

provides strong constraints for the theoretical models to be improved, especially now the uncertainties are smaller due to the combining of the 2015 and 2018 datasets. The two plots below are averaged for all D mesons to provide even further insight. The same conclusions can be drawn from these figures meaning that the D^{*+} R_{AA} calculated in this thesis is comparable to the average of D mesons that is calculated by the ALICE collaboration.
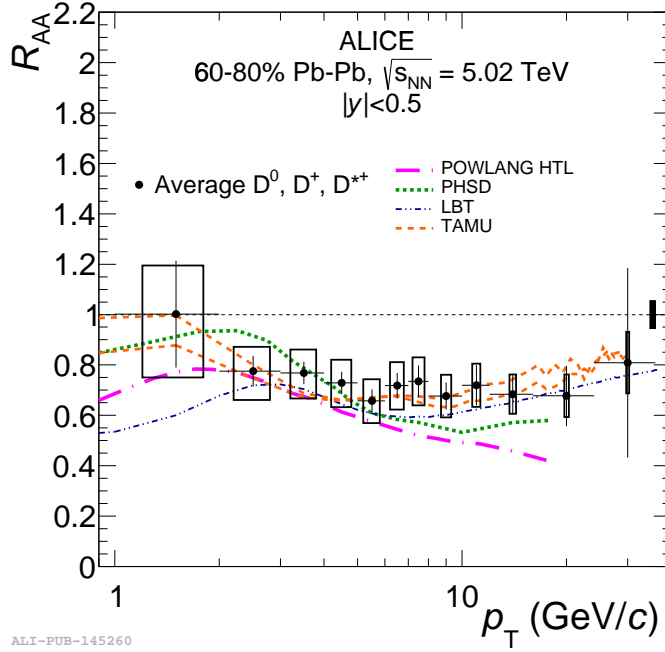

Figure 5.6 – Model comparisons including the other D mesons
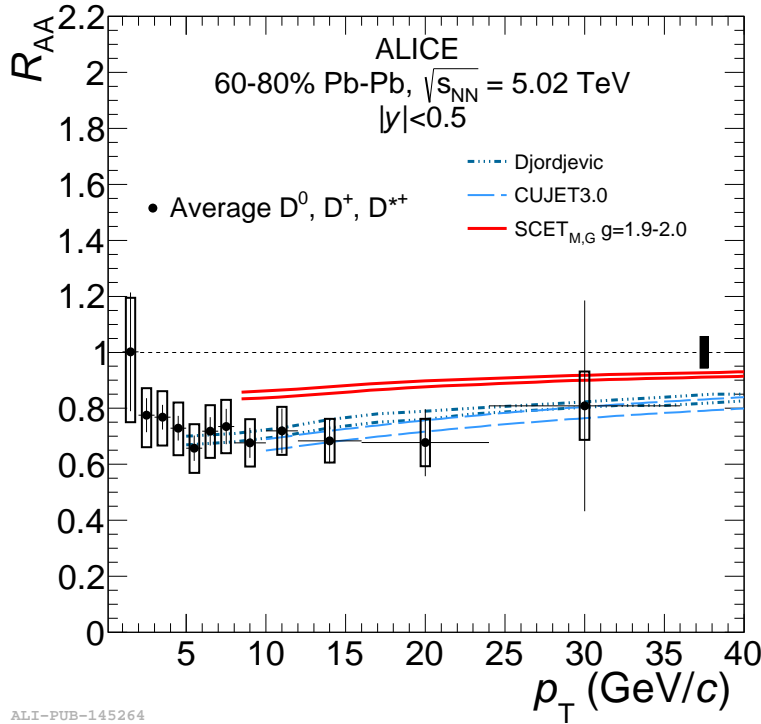

Figure 5.7 – Model comparisons including the other D mesons

Chapter 6

Discussion, Conclusion and outlook

To conclude, it can be stated that the nuclear modification factor R_{AA} in this thesis shows signs of suppression in the intermediate p_T ranges. When comparing the results from p-p an p-Pb as can be seen in the image below, these nuclear effects that produce the suppression are only seen in Pb-Pb collisions.

ALI-PUB-321163
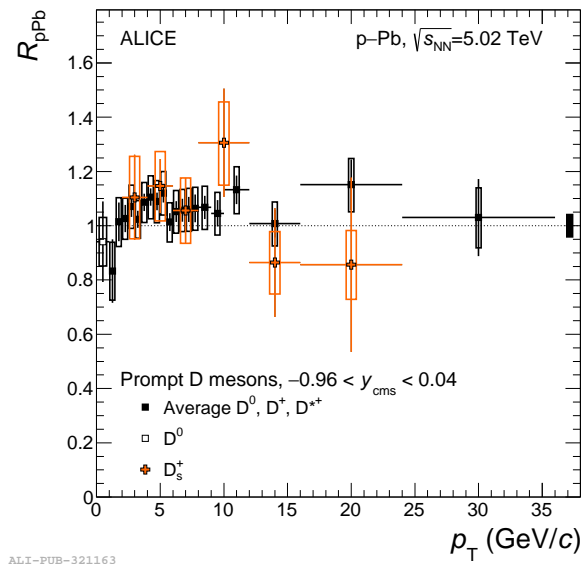
This shows that in Pb-Pb, nuclear effects that can be attributed to the formation of the Quark Gluon Plasma are found. When compared to different centrality classes, it can be stated that there is a hint of ordering between the centrality classes with a stronger suppression found in the more central collisions.

To improve the measurements and accuracy of the calculation, an anchored MC dataset would be desired. While there was a strong overlap between the 2018 dataset and the MC dataset used in 2015, an anchored dataset will give more precision in comparing the data to MC. The production of this MC dataset is not prioritised now but will probably be available somewhere in the future.

An upgraded ALICE detector and especially an upgraded ITS will give more certainty on the data that is gathered. Not only will there be more data available to study, the precision of tracking using the upgraded ITS will further reduce background.

Chapter 7

Appendix A

- **LHC18q_pass1 :** 296623, 296622, 296621, 296619, 296618, 296616, 296615, 296594, 296553, 296552, 296551, 296550, 296549, 296548, 296547, 296516, 296512, 296511, 296510, 296509, 296472, 296433, 296424, 296423, 296420, 296419, 296415, 296414, 296383, 296381, 296380, 296379, 296378, 296377, 296376, 296375, 296312, 296309, 296304, 296303, 296280, 296279, 296273, 296270, 296269, 296247, 296246, 296244, 296243, 296242, 296241, 296240, 296198, 296197, 296196, 296195, 296194, 296192, 296191, 296143, 296142, 296135, 296134, 296133, 296132, 296123, 296074, 296066, 296065, 296063, 296062, 296060, 296016, 295942, 295941, 295937, 295936, 295913, 295910, 295909, 295861, 295860, 295859, 295856, 295855, 295854, 295853, 295831, 295829, 295826, 295825, 295822, 295819, 295818, 295816, 295791, 295788, 295786, 295763, 295762, 295759, 295758, 295755, 295754, 295725, 295723, 295721, 295719, 295718, 295717, 295714, 295712, 295676, 295675, 295673, 295668, 295667, 295666, 295615, 295612, 295611, 295610, 295589, 295588, 295586, 295585

- **LHC18r_pass1:** 297595, 297590, 297588, 297558, 297544, 297542, 297541, 297540, 297537, 297512, 297483, 297481, 297479, 297452, 297451, 297450, 297446, 297442, 297441, 297415, 297414, 297413, 297406, 297405, 297380, 297379, 297372, 297367, 297366, 297363, 297336, 297335, 297333, 297332, 297317, 297311, 297310, 297278, 297222, 297221, 297218, 297196, 297195, 297193, 297133, 297132, 297129, 297128, 297124, 297123, 297119, 297118, 297117, 297085, 297035, 297031, 296966, 296941, 296938, 296935, 296934, 296932, 296931, 296930, 296903, 296900, 296899, 296894, 296852, 296851, 296850, 296848, 296839, 296838, 296836, 296835, 296799, 296794, 296793, 296790, 296787, 296786, 296785, 296784, 296781, 296752, 296694, 296693, 296691, 296690

Chapter 8

Appendix B

- **LHC16i2c** Runlist 1: 245833, 245949, 245952, 245954, 246003, 246012, 246053, 246751, 246765, 246766, 246810, 246989, 246991, 246994 Runlist pass1: 246994, 246991, 246989, 246984, 246982, 246948, 246945, 246928, 246851, 246847, 246846, 246845, 246844, 246810, 246809, 246808, 246807, 246805, 246804, 246766, 246765, 246763, 246760, 246759, 246758, 246757, 246751, 246750, 246495, 246493, 246488, 246487, 246434, 246431, 246424, 246276, 246275, 246272, 246271, 246225, 246222, 246217, 246185, 246182, 246181, 246180, 246178, 246153, 246152, 246151, 246115, 246113, 246089, 246087, 246053, 246052, 246049, 246048, 246042, 246037, 246036, 246012, 246003, 246001, 245954, 245952, 245949, 245923, 245833, 245831, 245829, 245705, 245702, 245692, 245683 Runlist pass1 pidfix: 245145, 245146, 245148, 245151, 245152, 245231, 245232, 245259, 245343, 245345, 245346, 245347, 245349, 245353, 245396, 245397, 245401, 245407, 245409, 245410, 245411, 245439, 245441, 245446, 245450, 245452, 245454, 245496, 245497, 245501, 245504, 245505, 245507, 245535, 245540, 245542, 245543, 245544, 245545, 245554 Runlist pass3 lowIR: 244918, 244975, 244980, 244982, 244983, 245061, 245064, 245066, 245068, 246390, 246391, 246392 Runlist IRlt4: 246994, 245954, 246991, 246012, 245952, 245833, 245949, 246766, 246765, 246989, 246003, 246810, 246053, 245705, 246089, 245831, 246763, 246276, 245702, 245152, 245151, 245146, 245145, 245232, 245148, 245411, 245410, 245454, 245259, 245409, 245507, 245554, 245452, 245505, 245407, 245353, 245450, 245504, 245545, 245544, 245446, 245349, 245501, 245401, 245543, 245441, 245347, 244918, 245068, 245066, 244983, 244982, 245064, 244980, 244975, 246391, 246390, 246392, 245061 Runlist IRgt4: 246185, 246495, 246052, 246225, 246809, 246153, 246275, 246760, 246493, 246182, 246049, 246001, 245829, 246759, 246808, 246222, 245692, 246152, 246984, 246758, 246048, 246807, 246181, 246087, 246272, 246757, 246434, 246151, 246042, 246488, 246804, 246948, 246982, 246846, 246928, 246115, 246945, 246180, 246805, 246217, 246851, 245683, 246847, 246750, 246751, 246271, 246487, 246431, 246844, 246037, 246178, 246845, 246424, 245923, 246113, 246036, 245231, 245397, 245542, 245497, 245346, 245540, 245439, 245496, 245396, 245345, 245535, 245343

Bibliography

[1] CERN article on Higgs boson and Higgs field https://home.cern/science/physics/higgs-boson

[2] Dark Energy, Dark Matter by CERN, https://home.cern/science/physics/dark-matter, 2016

[3] Particle Data Group on quark mass http://pdg.lbl.gov/2017/reviews/rpp2017-rev-quark-masses.pdf

[4] Frank Wilczek, *QCD Made Simple*, Physics Today, 2000

[5] Schematical overview of Standard Model https://www.quantumuniverse.nl/quantumfysica-14-het-standaardmodel

[6] Experimental tests of asymptotic freedom S.Bethke

[7] Manuel Caldern de la Barca Snchez, *Phase diagram QGP*, https://www.bnl.gov/rhic/news/050807/story1.asp, 2007

[8] F.-M. Liu and S.-X. Liu, Phys. Rev. C89 no. 3, (2014) 034906, arXiv:1212.6587.

[9] R. Baier, Y. L. Dokshitzer, A. H. Mueller, S. Peigne, and D. Schi, Nucl.Phys. B484 (1997) 265282, arXiv:hep- ph/9608322.

[10] M. Gyulassy and M. Plumer, Phys.Lett.B243 (1990) 432438

[11] Taken from slides Syaefudin Jaelani at SQM 2019 https://indico.cern.ch/event/755366/

[12] N. Armesto, C. A. Salgado and U. A. Wiedemann, Phys. Rev. D 69 (2004) 114003.

[13] ALICE figure repository http://alice-figure.web.cern.ch/published_fig

[14] E. Braaten, M. H. Thoma, Phys. Rev. D 44, no. 9, R2625 (1991)

[15] Baier et al. Nucl. Phys. B 483 (1997) 291-320

[16] Chun Shen and Ulrich Heinz ,The Road to Precision: Extraction of the Specific Shear Viscosity of the Quark-Gluon Plasma, Nuclear Physics News, 25,2 (2015) https://doi.org/10.1080/10619127.2015.1006502

[17] LHC figures and facts https://home.cern/resources/brochure/accelerators/lhc-facts-and-figures

[18] Florent Fayette, *Strategies for precision measurements of the charge asymmetry of the W boson mass at the LHC within the ATLAS experiment*, http://inspirehep.net/record/823897/plots, 2009

[19] ALICE experiment https://home.cern/science/experiments/alice

[20] CERN site https://cds.cern.ch/record/2646381?ln=en

[21] F. Carnesecchi [ALICE Collaboration], [arXiv:1806.03825 [physics.ins-det]].

[22] Root Analysis framework https://root.cern.ch/

[23] Github with ALICE macros https://github.com/alisw/AliPhysics

[24] ALICE LEGO train system https://alice-doc.github.io/alice-analysis-tutorial/analysis/lego.html#the-lego-train-system

[25] ALICE monitor system for LEGO trains http://alimonitor.cern.ch/map.jsp

[26] R. Brun et al., GEANT Detector Description and Simulation Tool https://doi.org/10.17181/CERN.MUHF.DMJ1

[27] T. Sjstrand, S. Mrenna and P.Z. Skands, PYTHIA 6.4 Physics and Manual JHEP05(2006)026[hep-ph/0603175

[28] Data Preparation Group http://alice-offline.web.cern.ch/Activities/alice-data-preparation-group

[29] The ALICE collaboration Measurement of D 0 , D + , D + and D + s production in PbPb collisions at s NN = 5.02 TeV https://doi.org/10.1007/JHEP10(2018)174

[30] Quality assurance of 2018 Pb-Pb data. https://indico.cern.ch/event/776522/

[31] http://pdg.lbl.gov/2019/listings/rpp2019-list-D-zero.pdf

[32] http://pdg.lbl.gov/2019/listings/rpp2019-list-D-star-2010-plus-minus.pdf

[33] M. Cacciari, M. Greco and P. Nason, The p T spectrum in heavy flavor hadroproduction JHEP05(1998)007[hep-ph/9803400]

[34] Uphoff, O. Fochler, Z. Xu and C. Greiner, Elliptic Flow and Energy Loss of Heavy Quarks in Ultra-Relativistic heavy Ion Collisions Phys.Rev.C84(2011)024908[arXiv:1104.2295]

[35] Presentation on Pile up corrections in 2018 Pb Pb data for the ALICE HF group https://indico.cern.ch/event/783268/

[36] PRC 92 (2015) 024918

[37] JHEP02(2016)169

[38] JHEP 03 (2017) 146

[39] EPJC 75 (2015) 121

[40] Phys. Lett. B735 (2014) 445

[41] 10.1016/j.physletb.2017.12.023

[42] [10]PRC 93 (2016) 03490